

The Dynamics of Poor Systems of Galaxies

Andisheh Mahdavi and Margaret J. Geller
Harvard-Smithsonian Center for Astrophysics

Hans Böhringer
Max-Planck-Institut für Extraterrestrische Physik

Michael J. Kurtz
Harvard-Smithsonian Center for Astrophysics

and

Massimo Ramella
Osservatorio Astronomico di Trieste

ABSTRACT

We assemble and observe a sample of poor galaxy systems that is suitable for testing N-body simulations of hierarchical clustering (Navarro, Frenk, & White 1997; NFW) and other dynamical halo models (e.g., Hernquist 1990). We (1) determine the parameters of the density profile $\rho(r)$ and the velocity dispersion profile $\sigma_p(R)$, (2) separate emission-line galaxies from absorption-line galaxies, examining the model parameters and as a function of spectroscopic type, and (3) for the best-behaved subsample, constrain the velocity anisotropy parameter, β , which determines the shapes of the galaxy orbits.

Our sample consists of 20 systems, 12 of which have extended x-ray emission in the ROSAT All-Sky Survey. We measure the 877 optical spectra of galaxies brighter than $m_R \approx 15.4$ within $1.5h^{-1}$ Mpc of the system centers (we take $H_0 = 100h$ km s $^{-1}$ Mpc $^{-1}$). Thus we sample the system membership to a radius typically three times larger than other recent optical group surveys. The average system population is 30 galaxies, and the average line-of-sight velocity dispersion is ≈ 300 km s $^{-1}$.

The NFW universal profile and the Hernquist (1990) model both provide good descriptions of the spatial data. In most cases an isothermal sphere is ruled out. Systems with declining $\sigma_p(R)$ are well-matched by theoretical profiles in which the star-forming galaxies have predominantly radial orbits ($\beta > 0$); many of these galaxies are probably falling in for the first time. There is significant evidence for spatial segregation of the spectroscopic classes regardless of $\sigma_p(R)$.

1. Introduction

Groups of galaxies have attracted astronomers since the days of Shapley (1933) and Zwicky (with Humason, 1960). Although the division between clusters and groups must have seemed natural early on—comparing the “rich” Coma Cluster, for example, with the “poor” Stephan’s Quintet—today the distinction is hardly obvious. A host of group catalogs (e.g., Albert, White, & Morgan 1977; Hickson 1982; Huchra & Geller 1982; Morgan & Hartwick 1988; Ramella, Geller, & Huchra 1989; Gourgoulhon, Chamaraux, & Fouque 1992; Ramella, Pisani, & Geller 1997; Trasarti-Battistoni 1998) make it clear that “groups” are often as well-populated as Abell’s (1958) clusters (to the same apparent magnitude limit), and are sometimes parts of richer, perhaps bound systems (e.g., Ramella et al. 1994; Barton, de Carvalho, & Geller 1998). The potpourri of adjectives with overlapping meanings still used to describe groups and clusters—“poor,” “rich,” “compact,” and “loose”—is a sign that the relationship among systems of galaxies across the full extent of their spectrum is not yet well understood.

Much of the literature on “groups” deals with an important initial difficulty in studying poor systems of galaxies: optically selected catalogs are likely to contain large numbers of apparent systems which are actually chance superpositions even though the member galaxies have similar redshifts (e.g., Walke & Mamon 1989; Hernquist, Katz, & Weinberg 1995). Detecting thermal bremsstrahlung x-ray emission from gas in the group potential increases the probability that galaxies in an overdense region form a bound system, (e.g., Schwartz, Schwarz, J., & Tucker, 1980; Ponman et al. 1996); however, if the large scale matter distribution is filamentary, the x-ray emitting gas as well as the galaxies may be projected onto a deceptively overdense region (Ostriker, Lubin, & Hernquist 1995). In conjunction with x-ray observations, obvious remedies against confusing the chance alignments with bound systems are to sample the overdense regions more deeply for additional associated galaxies (e.g., Zabludoff & Mulchaey 1998), and to identify additional group members within the neighboring few Mpc of the overdense region (e.g., Ramella et al. 1995).

There is a rich corpus of theoretical work on the dynamics of low-velocity dispersion systems. N-body simulations of isolated groups initialized in virialized states (Bode, Cohn, & Lugger 1993; Bode et al. 1994; Athanassoula, Makino, & Bosma 1997) indicate that dynamical friction plays an important role in the evolution of groups, and that the formation of a central, massive galaxy which continually accretes smaller group members is rapid. In this theoretical scenario dynamical equilibrium is out of the question because of the large and roughly constant frequency of galaxy interactions. The cosmological simulations of Nolthenius, Klypin, & Primack (1997) similarly show that only halos with

mass $> 10^{14} M_{\odot}$ are guaranteed to be virialized after a Hubble time; dynamical equilibrium is a poor description of less massive systems. However, Bahcall, Gramann, & Cen (1994) use their N-body simulations to claim that the velocity distribution of galaxies in groups is nearly Maxwellian, and Frederic’s (1995b) N-body code provides evidence that certain robust virial mass estimates applied to groups are accurate and unbiased. Whatever the truth of the matter, equilibrium models often form the basis for conclusions about the mass distribution in groups (e.g., Persic & Salucci 1992; Dell’Antonio, Geller, & Fabricant 1995; Pedersen, Yoshi, & Sommer-Larsen 1997; Zabludoff & Mulchaey 1998).

Literature which links real groups with theoretical work is less abundant. There has been some comparison of N-body simulations with observed group luminosity functions (LFs); Moore, Frenk, & White (1993), for example, find good agreement between group LFs and the results of their N-body simulations. Nolthenius, Klypin, & Primack (1994,1997) use other catalog statistics, such as the fraction of galaxies identified as group members, to constrain the cosmological parameters from N-body simulations; but Diaferio et al. (1999), whose simulations distinguish galaxies from dark matter halos, are able to reproduce the LFs of group catalogs largely independently of the cosmological parameters.

For lack of adequate group data, however, direct comparisons of real systems with theoretical density and velocity dispersion profiles exist only for rich clusters (e.g. Carlberg et al. 1997a,b). The goal of this paper is to model the internal dynamics of low-mass systems of galaxies by providing a catalog suited to the task.

We compare the optical properties of poor groups of galaxies with the Navarro, Frenk & White (1997) universal profile, which fits cosmological simulations of dark matter halos over many orders of magnitude in halo mass. We also examine the Hernquist (1990) profile, first derived to fit elliptical galaxies. Throughout the analysis we divide the system populations according to spectroscopic type by classifying the individual spectra as either absorption- or emission-line dominated; in this way we model the kinematics of galaxies with predominantly older stellar populations separately from those which have active star formation.

To test the models, it is necessary (1) to have a large enough (≈ 30) galaxy membership per system and (2) to sample the membership well outside the core in order to cover the tails of the theoretical distributions sufficiently. Previous catalogs of poor systems fulfill either the first (Pildis et al. 1995; Zabludoff & Mulchaey 1998) or the second (Ramella et al. 1995) criterion, but not both. In §2 we describe our assembly and observations of a catalog of groups, each with membership complete to roughly the same apparent magnitude ($m_R = 15.4$) within $1.5h^{-1}$ Mpc of the system center; in §3 we discuss an objective method for spectral classification of the member galaxies.

We identify system members in §4, and in §5 we determine the line-of-sight velocity dispersion profiles. We examine the behavior of the basic dynamical properties as a function of spectroscopic type in §6, and fit theoretical models in §7; in §8 we summarize.

2. The Data

We assemble and analyze a sample of galaxy systems, the Deep Optical Catalog or “DOC” hereafter. Two larger surveys are the sources of the DOC: (1) the Ramella et al. (1999) catalog of galaxy systems selected optically from the combined CfA–SSRS2 redshifts surveys (the “CSOC” hereafter; see below) and (2) the ROSAT All Sky Survey—Center for Astrophysics Loose Systems (the “RASSCALs” hereafter; Mahdavi et al. 1999), an x-ray emitting subset of the CSOC.

Figure 1 shows the relationship among the DOC, the CSOC, and the RASSCALs. All the systems in the DOC and the RASSCALs also belong to the CSOC; however the DOC contains more galaxies per system, and has a high quality optical spectrum for each galaxy.

2.1. Optical Source Catalog

The CfA–SSRS2 Optical Catalog (Ramella et al. 1999) is a sample of galaxy systems drawn objectively from two complete redshift surveys. It includes systems in a wide variety of dynamical states, from groups with ~ 5 members to the Coma cluster.

The Center For Astrophysics Redshift Survey (Geller & Huchra 1989; Huchra et al. 1990; Huchra, Geller, & Corwin 1995; Falco et al. 1999 CfA) and the smaller Southern Sky Redshift Survey (Da Costa et al. 1994; Da Costa et al. 1998), both complete to $m_B = 15.5$ ($m_R \approx 14.4$), served as sources for the CSOC. Systems in the CSOC bear the label of the redshift survey in which they are located; the names of systems we describe here begin with either NRG (northern CfA) or SRG (southern CfA). The portion of the CSOC we use covers more than one sixth of the sky in two separate sections: (1) NRG, $\alpha_{2000} = 8.5$ hours to 17 hours and $\delta_{2000} = 8.5^\circ$ to 43.5° , (2) SRG, $\alpha_{2000} = 21.5$ hours to 3 hours and $\delta_{2000} = -2^\circ$ to 32° .

Ramella et al. (1999) use a two-parameter method to construct the CSOC. Huchra & Geller (1982) first described this friends-of-friends algorithm (FOFA) for use with redshift surveys, and Ramella, Pisani, & Geller (1997; RPG) revised and applied it to the NRG data. The FOFA is a three-dimensional algorithm which identifies regions with a galaxy overdensity $\delta\rho/\rho$ greater than some specified threshold. A second fiducial parameter, V_0 , rejects galaxies in the overdense region which are too far removed in velocity space from their nearest neighbor. The N-body simulations of Frederic (1995a) show that the Huchra & Geller (1982) detection method misses few real systems, at the cost of including some spurious ones. Ramella et al. (1999) apply the FOFA to the combined NRG and SRG redshift surveys with $\delta\rho/\rho = 80$.

The CSOC contains 256 systems with $3000 \text{ km s}^{-1} \leq \langle v \rangle \leq 12000 \text{ km s}^{-1}$ and an average of 9 members galaxies per system. The low velocity cutoff rejects systems which cover a large area on the sky, and which may be affected by motions in the Local Group. The median recession velocity for systems in the CSOC is 7000 km s^{-1} ; therefore the effects of cosmology and evolution are negligible throughout the sample.

2.2. The X-Ray Data

Mahdavi et al. (1997; MBGR) describe a technique to search the ROSAT All-Sky Survey (Voges 1993; RASS) for low surface brightness x-ray emission from systems of galaxies. Mahdavi et al. (1999) apply the method, which uses optical galaxy positions to limit the sky area searched for emission, to all the groups in the CSOC with 5 or more members. They use a newly processed version of the survey (RASS II; Boller et al. 1998), which corrects effects leading to a low detection rate in the original reduction (RASS I).

The MBGR approach sums x-ray photons only within the union of all projected $0.4h^{-1}$ Mpc regions around each system member identified in the CSOC. This “position template” method has an advantage over traditional detection algorithms: it operates on unbinned, unsmoothed, raw counts, and as a result can detect much lower surface-brightness emission. The drawback of the MBGR method is that it can measure only the total integrated emission within the position template; any analysis of points sources like active galactic nuclei (AGN) must take place *post facto* with traditional techniques.

Using the position template method, Mahdavi et al. (1999) find that 101 of the CfA-SSRS2 systems have statistically significant x-ray emission in the RASS. In each case, they evaluate the probability P_{point} that the x-ray emission is due to a point source such as an active galactic nucleus (AGN). P_{point} results from a Kolmogorov-Smirnov Test (see §C) comparing the projected radial profile of the emission with that of the ROSAT PSPC point spread function. Systems with a high likelihood of having extended x-ray emission due to bremsstrahlung of hot gas in a potential ($P_{\text{point}} \lesssim 0.03$) make up the catalog of ROSAT All Sky Survey—Center for Astrophysics Loose Systems (RASSCALs).

2.3. The Current Sample of Groups

The Deep Optical Catalog (Table 1) consists of 20 systems. Of these, 12 are selected randomly from the subset of CSOC groups which (1) have extended ($P_{\text{point}} \leq 0.003$) x-ray emission, (2) have velocity dispersions $\sigma_p < 700 \text{ km s}^{-1}$, and (3) are observable from the 1.5

meter Tillinghast Reflector on Mt. Hopkins, Arizona. The remaining systems were selected randomly from the subset of CSOC groups which fulfill (2) and (3) above, but either have pointlike or no x-ray emission. The systems with extended x-ray emission have a higher likelihood of being bound than the rest, but the presence of this emission is no guarantee that the groups are virialized.

Because the CSOC systems are identified with objective overdensity and velocity difference criteria, the DOC is a representative sample of groups without implicit morphological selection biases. Our sample includes two Abell clusters, A779 and A1185. Figures 2–6 show the RASSCALs x-ray data for this sample.

MBGR analyzed the x-ray data for 10 of the DOC systems. However, the RASSCALs x-ray data differs somewhat from that of MBGR because (1) in MBGR the fields were not large enough to capture all the x-ray emission from some of the systems at low redshift, and therefore MBGR did not detect some of the RASSCALs, and (2) the RASSCALs x-ray data is from the more current reduction of the ROSAT All Sky Survey (RASS II). Mahdavi et al. (1999) discuss these issues in greater detail.

We used the high-throughput FAST spectrograph on the Tillinghast (Fabricant et al. 1998), which, with a 300 line mm^{-1} grating and a $3''$ slit, has a resolution of $\approx 1.5 \text{ \AA}$, and a spectral coverage of 3940 \AA , centered at 5500 \AA . For $z < 0.05$, the redshift neighborhood of interest for this work, the FAST allows us to measure the equivalent widths of emission lines which are important markers of star formation, from $[\text{O II}]$ at 3727 \AA to $\text{H}\alpha$ at 6563 \AA .

For each system we obtain digitized Palomar Observatory Sky Survey (POSS) positions for all galaxies with $m_R \lesssim 15.4$, which lie within a projected distance of $1.5h^{-1} \text{ Mpc}$ of the system center as defined in the CSOC. We use the FOCAS (Valdes et al. 1995) program to separate stars from galaxies, but we also check each field by eye to make sure FOCAS has not neglected any bright elliptical or edge-on spiral galaxies. We calibrate the FOCAS magnitudes to the R magnitude system by (1) finding all CSOC galaxies with measured B band magnitudes in each field, (2) applying a standard $B - R = 1.1 \text{ mag}$ color conversion, the average for elliptical and spirals (Frei & Gunn 1994) to each CSOC galaxy, and (3) using a linear fit to the corresponding FOCAS magnitudes to obtain the transformation for all galaxies in each field. We estimate that the scatter around the $m_R = 15.4$ completeness limit in each system is $\approx 0.3 \text{ mag}$, and that from system to system it is $\approx 0.5 \text{ mag}$.

After obtaining the positions, we measure the spectra of all galaxies with unknown redshifts, and remeasure the spectra of galaxies with a known CSOC redshift in the interval $|cz - \langle v \rangle| < 4000 \text{ km s}^{-1}$, where $\langle v \rangle$ is the recession velocity of the system under study. Therefore the members of all the systems in the DOC, and most of the foreground and

background galaxies, have high-quality FAST spectra complete to $m_R \approx 15.4$.

There are a total of 877 new galaxy spectra in the DOC; 154 of these are remeasurements of CSOC galaxies. We analyze the data with the spectroscopy package of the Image Reduction and Analysis Facility (Valdes 1992; IRAF), and derive redshifts using the RVSAO program (Kurtz et al. 1992; Kurtz & Mink 1998), which applies cross-correlation techniques to log-wavelength binned spectra (Tonry & Davis 1979). We use cross correlation for both emission and absorption spectra.

Table 2 lists the velocities. A sample page is included here; the entire table is available in electronic form.

3. Spectroscopic Classification

We use the optical spectrum of each galaxy to decide whether the galaxy is “absorption-dominated,” that is, consists mostly of an older stellar population (with metallic absorption lines that dominate the optical spectrum), or whether it is “emission-dominated” (with $H\alpha$, [O II] and other lines indicative of active star formation).

To classify each of the new FAST spectra, we first de-redshift it to the heliocentric rest frame $z = 0$. We fit a cubic spline to determine the continuum emission, which we subtract from the spectrum. Using only the portion between 3600–6900 Å, binned into 2200 channels of width 1.5 Å each, we fit the linear combination $C_e T_e + C_a T_a$ to the spectrum, where C_e and C_a are the dimensionless emission and absorption coefficients determined from the fit, and T_e and T_a are the template emission and absorption spectra, respectively.

These templates (Figure 7) are the same ones we use to determine the redshift with RVSAO cross-correlation methods. Kurtz & Mink (1998) describe the template construction procedure, which for T_e consists of averaging the profiles of the emission lines identified in a large number of emission-dominated galaxy spectra, and for T_a involves averaging a large number of pure absorption spectra. The template spectra have no continuum emission. Before fitting the templates to the FAST data we extract the 3600-6900 Å region. We bin the templates in the same way as we bin the data.

We use the generalized least squares procedure (Press et al. 1992) to fit the 738 galaxy spectra with $500 \text{ km s}^{-1} \leq cz \leq 15000 \text{ km s}^{-1}$. The distribution of χ^2/ν for the fits has a mean value of 1.49. Figure 8 shows the distribution of the parameters C_e and C_a . The 68.3% confidence errors are derived from the fit covariance matrix.

In Figure 8, the absorption-dominated galaxies cluster at the lower right corner, where C_e is zero. There is a smooth transition from this high density region to the emission-dominated galaxies, which rise towards the upper left corner of the figure. The emission-dominated population shows no clustering, because absorption lines from the older stellar population are detectable in almost all the galaxy spectra; thus most of the galaxies have $C_a \sim 1$.

Separating the two populations of galaxies is not straightforward, because their distribution does not show a clear break in the transition zone. Suppose, however, that there is a curve on Figure 8 which divides the populations in some maximum-likelihood sense. We would like to find this curve as objectively as possible, keeping in mind that some arbitrariness is inevitable. Luckily, a few physical considerations constrain the nature of the division:

1. The curve must be a function of the absorption coefficient with positive or zero first derivative. For suppose two galaxies have the same C_e , but different C_a ; and that the one with the smaller C_a is classified as absorption-dominated. Then necessarily the other galaxy must be classified the same way. A similar argument holds for C_e .
2. The curve must not classify galaxies with $C_e \leq 0$ as emission-dominated.
3. The curve must not classify galaxies with “large enough” C_e as absorption-dominated.

We separate the two galaxy populations on Figure 8 with a straight line $C_e = aC_a + b$ for simplicity. Condition (1) above requires $a \geq 0$. Condition (2), given our data, requires, $b > -0.6a$. Selecting $C_e = \mu_{C_e} + 3\sigma_{C_e} = 0.3$ as “large enough” (where μ_{C_e} is the mean and σ_{C_e} is the standard deviation of the 738 C_e ’s), condition (3) requires $a < 1.5$. The permitted region for a and b is now small enough to allow efficient numerical exploration.

To find the optimum values of a and b , we iterate over the permitted values, each time classifying galaxies with $C_e \leq aC_a + b$ as absorption-dominated, and the others as emission-dominated. We exclude two galaxies with anomalous coefficients $C_e \approx C_a \approx 0$ from this procedure. For each pair of populations we compute the two-dimensional KS statistic d_2 (see §C), which is a measure of the degree of difference between two populations; the larger d_2 , the more likely it is that the two populations have different distributions. The maximum value of d_2 therefore gives the maximum-likelihood combination of a and b .

Figure 9 shows a contour plot of d_2 in the region of maximum likelihood. The optimum values are $a = 0.02$ and $b = 0.038$; the fit parameters are stable (to within the uncertainties) as the sample size increases. Figure 8 shows the line which separates the two populations. About 53% of the galaxies lie below the line; these are “absorption-dominated” galaxies; the rest are “emission-dominated.”

4. Basic Dynamical Properties

Pisani (1993) developed a non-parametric, scale-independent method which picks out structure in a one-dimensional data set. Without making use of a histogram, it estimates the probability distribution function (PDF) underlying the data as a kernel f_{ka} which is a sum of Gaussians with widths optimized to the local sampling rate:

$$f_{ka}(v) \equiv \frac{1}{N} \sum_i^K K(cz_i, s_i, v) \quad (1)$$

$$K(cz_i, s_i, v) \equiv \frac{1}{\sqrt{2\pi}s_i} \exp \left[-\frac{(v - cz_i)^2}{s_i^2} \right] \quad (2)$$

Here N is the number of galaxies in the field, each with a redshift z_i . The kernel is “adaptive” because s_i changes for each data point.

The adaptive kernel f_{ka} is a maximum-likelihood estimator of the system PDF. Pisani (1993) uses numerical simulations to show that f_{ka} , a function with essentially N degrees of freedom, can accurately reconstruct even the most asymmetric and non-Gaussian velocity distributions. The kernel f_{ka} is particularly useful, because it provides an estimate of the probability that each galaxy in the field is a member of the system. We can therefore remove interlopers by discarding all galaxies with a large enough probability of belonging to the foreground or the background. Furthermore, whenever f_{ka} detects multiple peaks in the velocity distribution of a particular system, they are statistically significant substructures in velocity space.

Figures 10–12 show histograms of the field of each system alongside f_{ka} for that field. Our procedure for determining system membership is:

1. Select all galaxies within $\pm 4000 \text{ km s}^{-1}$ of the system velocity as listed in the CSOC.
2. Compute f_{ka} for these galaxies, as well as the probability that the i th galaxy is an isolated foreground or background object, $P_{i \in 0} \equiv K(cz_i, s_i, cz_i) / [f_{ka}(cz_i) N]$. Exclude all galaxies with $P_{i \in 0} > 0.5$ from further analysis. Note that a galaxy with $P_{i \in 0} < 0.5$ is not necessarily a system member; it is just “unisolated.” While the $P_{i \in 0} > 0.5$ cutoff is arbitrary, it corresponds well to traditional rejection algorithms, for example 3- σ clipping.
3. Divide f_{ka} into ν_{tot} peaks by using its minima as delimiters. The galaxies are therefore also divided into ν_{tot} bins; the i th galaxy belongs to the ν th peak ($i \in \nu$).

4. From f_{ka} compute the probability that the i th galaxy belongs to peak ν :

$$P_{i \in \nu} \equiv \frac{1}{N f_{ka}(cz_i)} \sum_{j \in \nu, j \neq i} K(cz_j, s_j, cz_i) \quad (3)$$

5. Initially define the system membership as the peak ν_{max} with the most galaxies. However, if neighboring peaks have galaxies with a non-negligible probability of belonging to the main peak ($P_{\in \nu_{max}} > 0.003$), include these peaks in the system membership.

Figures 2–6 show sky plots of the members of each system, along with foreground and background galaxies and x-ray emission contours.

After establishing the membership, we compute centers for each system. If there is a single peak in the x-ray emission and it is associated with member galaxies, we choose the center of the x-ray peak as the system center. If, however, the system has multiply-peaked, irregular, or no x-ray emission, we use the average right ascension and declination of the optically identified members. In a few cases this process moves the circle of radius $1.5h^{-1}$ Mpc away from the CSOC center, excluding some galaxies with measured spectra from the region of interest, and therefore from the membership.

Finally, we compute the system recession velocity $\langle v \rangle$ and the line-of-sight velocity dispersion σ_p . In §D we test various robust methods of deriving these quantities; we find that the mean velocity \bar{v} and the standard deviation $\sqrt{\text{Var}(v)}$ are as effective as the robust estimators.

There is a rich qualitative variation in the relationship between the system membership and nature of the x-ray emission:

1. Of the 12 systems with significant extended x-ray emission, six (SRGb119, NRGb032, NRGb045, NRGb244, NRGb251, and SRGB009) are characterized by a single x-ray emitting region which is relatively round and symmetric. Of these systems, five have either one or two bright elliptical galaxies at the peak of the x-ray emission: NRGb032 (two), NRGb244 (one), NRGb251 (one), SRGB009 (two), and SRGB119 (two). These systems increased their membership to three times the original CSOC count or better. The system without a bright elliptical, NRGb045, increased its membership by a factor of 1.6. Thus there is some indication that the presence of a bright elliptical galaxy at the x-ray core correlates with richness. The differences in the population increase are not due to uncertainty in the magnitude limit.

2. The remaining systems with extended x-ray emission, SRGb062, NRGb025, NRGs117, NRGb247, NRGs385, and SRGb016, have irregular or multiple x-ray emission contours; all these systems more than tripled their original CSOC membership after our deeper sampling.
3. Of the 8 systems without statistically significant extended x-ray emission, one (NRGb043) more than quintupled its original CSOC membership; this system is probably bound, and may emit below the RASS detection threshold. The rest (NRGb007, NRGb004, NRGb057, NRGs127, NRGs156, NRGb181, and NRGs317) less than doubled the original count. Because these seven systems lack extended x-ray emission, and did not change their membership significantly after our survey, they may be artifacts of the FOFA algorithm. However, the deeper sampling does reveal a central condensation in both NRGb004 and NRGs317; it is therefore still not out of the question that these systems might be real groups which have x-ray emission undetectable in the RASS.

5. Velocity Dispersion Profiles

5.1. On the Virial Radius

In the literature describing N-body simulations of systems of galaxies (e.g., Navarro, Frenk, & White 1997), it is customary to show the dynamical properties as a function of r_{200} , the radius which contains an overdensity $200\rho_{\text{crit}}(z)$ (Navarro, Frenk, & White 1997; NFW), where $\rho_{\text{crit}}(z) = 3H_0^2(1+z)^3/(8\pi G)$ is the critical density of an Einstein-de Sitter universe at a redshift z .

Unfortunately, r_{200} is not straightforward to derive observationally. One method (Carlberg et al. 1997a,b) is to assume that the virial theorem holds:

$$M \equiv \alpha \sigma_p^2 r_v G^{-1}. \quad (4)$$

Here r_v is the virial radius, G is Newton’s gravitational constant, and α is a constant which depends on the orbit distribution of the system. Carlberg et al. (1997a,b) use $\alpha = 3$, appropriate for an isotropic distribution. The next step is to assume that the mass inside a radius r is proportional to r : $M(r) \propto r$. Then equation (4) with $\alpha = 3$ for a system at redshift z implies

$$\frac{\frac{4}{3}\pi r_{200}^3 \times 200\rho_{\text{crit}}(z)}{M_v} = \frac{r_{200}}{r_v} \quad (5)$$

$$100r_{200}^2 \frac{H_0^2}{G}(1+z)^3 = \frac{M_v}{r_v} \quad (6)$$

$$r_{200} = \frac{\sqrt{3}\sigma_p(1+z)^{-3/2}}{10H_0} \quad (7)$$

$$= \frac{\sigma_p(1+z)^{-3/2}}{577 \text{ km s}^{-1}} h^{-1} \text{ Mpc}. \quad (8)$$

The (usually neglected) $\sim 20\%$ uncertainty in σ_p translates into the same error in r_{200} . This loss of accuracy is significant considering that practically the only source of error in the projected radius R is the uncertainty in the determination of the center, when R is measured in Mpc.

The following are drawbacks in deriving the observational r_{200} from the virial theorem:

1. If the orbits are anisotropic, $\alpha = 3$ is incorrect by up to a factor of two.
2. If $M(r)$ is not proportional to r , the observational r_{200} is inappropriate. NFW’s “universal” density profile, for example, predicts $M(r) \propto r^2$ for small radii and

$M(r) \propto \ln[r/(r_{ce})]$ for large radii. Carlberg et al. (1997a,b) show that this profile adequately describes rich clusters of galaxies; below (see §7) we find that it also fits our groups well, whereas an $M(r) \propto r$ profile is ruled out in most cases.

3. Finally, the virial theorem may not apply to some of the systems in the sample. Even systems with extended x-ray emission are not guaranteed to be virialized. Substructure generally bloats, and infall generally compresses the line-of-sight velocity dispersion with respect to its equilibrium value. For example, the value of $r_{200} = 1.2h^{-1}$ Mpc for NRGs117 is probably too large, because this system has three subcondensations (Mahdavi et al. 1996). Similarly, $r_{200} = 0.12h^{-1}$ Mpc for NRGb045 is unlikely to be a true description of the overdensity radius, because $\sigma_p = 70$ km s $^{-1}$, from which it is derived, is smaller than the internal velocity dispersion of an L^* elliptical galaxy!

5.2. The Shapes of the Profiles

Figures 10–12 give a qualitative idea of the velocity dispersion as a function of projected radius. We divide the data for each group into three bins, containing the galaxies removed 0–0.5 h^{-1} Mpc, 0.5–1.0 h^{-1} Mpc, and 1.0–1.5 h^{-1} Mpc from the center, respectively, and compute the velocity dispersion for each of these bins.

Figure 13 shows the velocity dispersion profile $\sigma_p(R)$ for each system with $N > 10$ members. We compute $\sigma_p(R)$ by sorting the members in R , and then computing the velocity dispersion of a moving group of 9 galaxies, from the center out to a distance of $1.5h^{-1}$ Mpc. Every ninth point in the Figure 13 is statistically independent. We compute the errors by performing the bootstrap analysis described in §B on each bin.

The behavior of $\sigma_p(R)$ suggests that our sample consists of systems in a wide variety of dynamical states. The line-of-sight velocity dispersion profile, for example, rises in certain cases, falls in other cases, and sometimes just varies irregularly. The systems which have the most nearly constant $\sigma_p(R)$ —NRGs317, NRGb057, and NRGb004—are also the systems which have the fewest members; in these cases we may not be sampling the cores or outer regions sufficiently to detect a variation. Interestingly, these three systems also have x-ray emission which has a large probability of being due entirely to a point source ($P_{\text{point}} \geq 0.055$), and therefore have a smaller likelihood of being bound than the systems with clearly extended x-ray emission.

To examine the variation among the $\sigma_p(R)$ quantitatively, we perform the KS2D test (see §C) for the 105 unique pairs of systems with $N > 15$ members. Table 3 shows the

test results separately for R in units of Mpc and r_{200} . In both cases, for 41% of the unique system pairs in our sample, we can rule out the null hypothesis that $\sigma_p(R)$ is drawn from the same distribution at better than the 99.0% confidence level.

The data show, therefore, that our galaxy systems are not, as a rule, in similar dynamical states, because their velocity dispersion profiles often differ significantly. If we had followed Zabludoff & Mulchaey (1998) or Carlberg et al. (1997), for example, in pooling all our data, we would have averaged away the distinctive rising, falling, and irregularly varying individual profiles.

On the one hand, a few of our systems have profiles that qualitatively match recent N-body simulations of relaxed systems of galaxies as well as the analytical models we describe below (see §7). In SRGb009, SRGb016, NRGb032, SRGb062, and NRGb247, $\sigma_p(R)$ resembles the velocity dispersion profiles which Crone, Evrard, & Richstone (1994) compute for simulated clusters in various cosmologies. The characteristic rise which all the Crone et al. (1994) models exhibit within the first $\approx 0.2r_{200}$ is present in SRGb009 and NRGb247, and $\sigma_p(R)$ declines for all five systems out to $\approx 2r_{200}$, following the Crone et al. (1994) models. We will treat these systems, which have consistent distributions according to the KS2D test, as a special subsample (“Sample-D”). The x-ray emission in these systems is almost unquestionably extended ($P_{\text{point}} \leq 0.001$), another indication that they constitute a subsample which lends itself to clean dynamical modeling.

On the other hand, across our sample, $\sigma_p(R)$ does not exhibit the regularity which it should if all our systems were in dynamical equilibrium, or if their members had similar families of orbits. Our results are consistent with recent observational studies of clusters of galaxies, (e.g. Girardi et al. 1996), which show that even a sample of systems with $\sigma_p \sim 1000 \text{ km s}^{-1}$ exhibit both rising and falling velocity dispersion profiles within $1.5h^{-1}$ Mpc ($\approx 2h^{-1}r_{200}$). Substructure, anisotropies in the true three-dimensional velocity distribution, and differences in the dark matter mass profiles, together or individually, may explain the variations among $\sigma_p(R)$ for different systems of galaxies.

We suggest that in the systems with declining $\sigma_p(R)$ in the central region, the galaxies have mainly radial orbits, which bloat the radial velocity dispersion near the core, and shrink it at the outer edges. If this is the case, the galaxies could not have made many orbits; with a typical velocity of $\sim 200\text{--}400 \text{ km s}^{-1}$, they travel only $2h^{-1}\text{--}4h^{-1}$ Mpc in a Hubble time, sufficient to make just one crossing of the system diameter. It is therefore possible that a significant fraction of the galaxies are falling towards the system center for the first time. In §7 we will examine this scenario more rigorously, and consider the line-of-sight velocity dispersion profiles as a function of spectroscopic type.

6. Spectroscopic Segregation

Elliptical and S0 galaxies in clusters tend to be more centrally condensed than spiral galaxies, an effect related to the morphology-density relation in the nearby universe (e.g., Dressler 1980; Postman & Geller 1984; Lahav & Saslaw 1992; Whitmore, Gilmore, & Jones 1993; Anderson 1996). Some authors (e.g., Carlberg et al. 1997) separate populations by color and refer to “red” and “blue” galaxies instead. Sometimes, elliptical or “red” galaxies also have a lower velocity dispersion than the remaining system members (e. g., Stein 1996; Colless & Dunn 1996; Mohr et al. 1996). Together, these two effects may imply that many systems perhaps contain virialized cores of galaxies with older stellar populations, with the star-forming “blue” spirals being more recent, infalling additions to the system. Our spectral classes correspond only roughly to morphological or color classifications; however, we seek to establish whether the stellar populations of galaxies vary with distance from the system center in a way similar to the morphology or the color.

We compute $\langle v \rangle$, σ_p , and the average distance from the system center, \bar{R} , as a function of spectroscopic type. Hereafter we use a superscript a with each of these quantities for absorption-dominated galaxies only, a superscript m for emission-dominated galaxies only, and no superscript for each system as a whole. We exclude NRGs127, a system without x-ray emission, from our tests, because it contains only one emission-dominated galaxy.

We compare the distributions of emission-dominated and absorption-dominated galaxies with the Student’s t Test, which evaluates the probability that two populations have the same mean, and the F Test, which evaluates the probability that two populations have the same variance. When we apply the tests to individual systems, we use the measured velocities cz_i in km s^{-1} and projected distances R_i in Mpc from the center. Because scaling the data by a constant does not affect the outcome of either the Student’s t or the F Test, it is only necessary to normalize the velocities and radii when we compare the absorption-emission populations across several systems in our sample.

Therefore, when we pool together systems which have similar dynamical properties, we consider the normalized velocity v_i/σ_p in place of cz_i , and measure R_i in units of r_{200} as well as Mpc. We consider several pooled samples: “ALL” refers to all the galaxies which are system members; “Sample-A” refers to all the galaxies except the members of NRGs117 (A1185), a cluster with significant substructure (Mahdavi et al. 1996) which contains 14% of all the member galaxies, and therefore might significantly bias the test results; “Sample-D” refers to the systems with declining velocity dispersion (§5.2); and “Sample-I” refers to all systems not belonging to Sample-D (and excluding NRGs117). Table 4 shows the test outcomes; Figure 14 shows the velocity and radius distribution of the galaxies in each system as a function of spectroscopic type.

The tests unambiguously show that our data recover a “spectroscopic segregation” which resembles the morphology-density relation if we identify absorption-dominated galaxies with the elliptical or “red” members. With better than 99.9% confidence, \bar{R}^a is different from \bar{R}^m when we pool all system members together and measure R in Mpc. On the average, the absorption-dominated galaxies are $0.14h^{-1}$ Mpc closer to the system center than the emission-dominated galaxies. On an individual basis, nearly all the systems have $\bar{R}^a - \bar{R}^m < 0$; the two exceptions, NRGb007 and NRGb025, have $\bar{R}^a = \bar{R}^m$ within the uncertainties. When we measure R in units of r_{200} , the significance of the effect for the ALL sample drops to 99.0%. The physical units (Mpc) preserve the spectroscopic segregation relation more cleanly; the difference in physical scale among our systems is therefore smaller than error introduced into r_{200} through the uncertainty in σ_p ; see equation (8).

The velocity dispersions of the absorption- and emission-dominated populations, however, show no sign of segregation. NRGs117 is the only system for which $P(F)$ (the probability that two samples are drawn from distributions with the same variance) is small. The results of all the velocity tests for the combined subsamples are negative.

7. Comparison with Theory

Here we compare the data with spherically symmetric density models from N-body simulations and the theoretical literature. We have shown (§5.2) that one particular subsample, Sample-D, contains groups with statistically consistent velocity dispersion profiles. These groups also have similar global velocity dispersions $\sigma_p = 327\text{--}466 \text{ km s}^{-1}$, for which the variation in r_{200}^{Virial} is comparable to its uncertainty. While in this section we focus most of our analysis on Sample-D, we also consider separately (1) the subsample of high velocity dispersion ($\sigma_p > 350 \text{ km s}^{-1}$) systems, and (2) the subsample of low velocity dispersion ($\sigma_p < 350 \text{ km s}^{-1}$) systems.

We consider spherically symmetric density profiles of the form

$$\rho(r) = \frac{3M_c}{\Xi(\alpha)4\pi r_c^3} \left[\frac{r}{r_c} \left(1 + \frac{r}{r_c} \right)^\alpha \right]^{-1} \quad (9)$$

where r_c is the core radius, M_c is the mass within the core radius, and $\Xi(\alpha)$ ensures $\int_0^{r_c} 4\pi r^2 \rho(r) dr = M_c$. The model with $\alpha = 3$ is due to Hernquist (1990), who originally formulated it as a description of elliptical galaxies. The $\alpha = 2$ model is the universal profile of Navarro, Frenk, & White (1996; NFW), who use it as a fitting function to their simulations of collapsed halos in various cosmologies. The $\alpha = 2$ model is a good fit to the NFW simulations regardless of the cosmological parameters. The models have normalizations $\Xi(3) = 3/8$ and $\Xi(2) = 3 \ln(4/e)/2$, respectively. We also consider the singular isothermal sphere (SIS), which has $M(r) \propto r$ and $\rho(r) \propto r^{-2}$.

Carlberg et al. (1997b) also fit these models to their sample of 16 high-luminosity x-ray clusters. Here we compare the models for the first time to a sample consisting primarily of groups of galaxies. Our approach differs somewhat from that of Carlberg et al. (1997b): below we compute the three-dimensional radial velocity dispersion profile analytically from the Jeans equation, rather than adopting a fitting function with four free parameters.

For the sake of coherence among the model parameters, our notation for $\rho(r)$ is somewhat different from that of Hernquist (1990), NFW, and Carlberg et al. (1997a,b). Because the NFW model has a logarithmically divergent cumulative mass $M(r)$ as $r \rightarrow \infty$, NFW define the total halo mass as $M_{200} = 200\rho_{\text{crit}}(4\pi/3)r_{200}^3$, where $r_{200} = cr_c$ is the radius which contains 200 times the critical density of the universe, and c is the NFW halo “concentration.” NFW find that the concentration varies inversely with the mass of the halo. We instead use the mass inside r_c , which is more simply defined for both the NFW and the Hernquist (1990) models, for the profile normalization.

7.1. Surface Number Density Profiles

To fit the models to the optical data, we assume that galaxies trace mass. Then the three-dimensional galaxy number density is

$$n(r) = \frac{N_c}{M_c} \rho(r), \quad (10)$$

where N_c is the number of galaxies within the sphere of radius r_c . Our best fit N_c has a dependence on the $m_R \approx 15.4$ magnitude limit; the best fit r_c should be independent of this limit if the mass-to-light ratio is constant throughout each system. The quantity N_c is a superior fitting parameter to the core density $n_c \equiv 3N_c/(4\pi r_c^3)$, because fitting for n_c and r_c , as Carlberg et al. (1997a,b) effectively do, results in an unacceptably large correlation between the parameters. In our experience, including the directly observable parameters as explicitly as possible in the models to be fit results in a smaller correlation among the parameters.

The projection of equation (10) for $\alpha = 3$ is the surface number density profile,

$$\Sigma_3(\tilde{R}) = \frac{2N_c}{\pi r_c^2 (\tilde{R}^2 - 1)^2} \left[(2 + \tilde{R}^2) X(\tilde{R}) - 3 \right], \quad (11)$$

and for $\alpha = 2$ it is

$$\Sigma_2(\tilde{R}) = \frac{N_c}{\pi \ln(4/e) r_c^2 (\tilde{R}^2 - 1)} \left[1 - X(\tilde{R}) \right], \quad (12)$$

where $\tilde{R} = R/r_c$ is the projected radius in units of the core radius, and

$$X(\tilde{R}) = \frac{\sec^{-1} \tilde{R}}{\sqrt{\tilde{R}^2 - 1}}. \quad (13)$$

Note that $X(\tilde{R})$ is always real; for computation we use $\text{sech}^{-1} \tilde{R} = i \sec^{-1} \tilde{R}$ when $\tilde{R} < 1$. Also note that $\Sigma_3(1) = 8N_c/(15\pi r_c^2)$ and $\Sigma_2(1) = N_c/[3 \ln(4/e) \pi r_c^2]$. For the singular isothermal sphere, the surface density has the simple behavior $\Sigma_{\text{SIS}} \propto R^{-1}$.

To fit models, we use 20 bins, with an approximately equal number of galaxies n_{bin} per bin per fit, so that the fractional Poisson error $(\sqrt{n_{\text{bin}}} \ln 10)^{-1}$ in each bin is roughly constant. However, if this fractional error is greater than 15%, we decrease the number of bins and increase n_{bin} until the fractional error is smaller than 15%. We conduct two sets of fits: (a) measuring R in units of r_{200}^{Virial} , given by equation (8) (in which case $r_c = 1/c$ is dimensionless and equal to the inverse of the concentration); and (b) measuring R in units of Mpc. The χ^2 function is well-behaved and has, in each case, a unique minimum; we

compute it over a fine grid around the minimum, and assume that the large-count Gaussian limit of the Poisson distribution describes our errors when we show the 68.3% and 95.4% confidence contours. Figures 15–17 show the results of the fits for Sample-D, which we carry out in the $\log R - \log \Sigma$ plane. We list the parameters for fits to other subsamples in Table 5.

The following are the outstanding properties of the fits:

1. Both the Hernquist (1990) and NFW models provide good descriptions of the data. The isothermal sphere with $M(r) \propto r$ is usually the worst fit, and is often ruled out.
2. The fits are of much higher quality when we measure R in units of Mpc than when we use r_{200}^{Virial} ; the χ^2/ν is always smaller. We conclude that the uncertainties discussed above (§5.1) make a large contribution to the r_{200}^{Virial} , and this quantity is therefore a poor estimator of the true r_{200} for poor systems of galaxies. Classifying systems by the behavior of $\sigma_p(R)$ (§5.2) is probably a more effective way to identify dynamically similar groups.
3. The NFW concentration parameter c for Sample-D ($\sigma_p = 327\text{--}466 \text{ km s}^{-1}$) is 4.3–9.1 (one-dimensional 95.4% confidence interval); the corresponding value for rich clusters, as derived by Carlberg et al. (1997a), is 2.3–7.7. In their simulations NFW find that low-mass halos should have larger concentrations than high-mass ones; our results for Sample-D, taken together with those of Carlberg et al. (1997a,b), are consistent with that prediction.
4. The best-fit core radii r_c for the high- and low- σ_p systems would seem to contradict the NFW picture. If the low- σ_p systems are truly less massive than their high- σ_p counterparts, then NFW predict $c_l > c_h$ as well as $r_{200,l} < r_{200,c}$. Substituting the definition of the concentration, we have $r_{c,l} < r_{c,h}$, which is not favored by the combined fit parameters listed in Table (5). We are nevertheless still faced with the fact that the NFW profile fits both subsamples well. Perhaps the internal inconsistency of the high- and low- σ_p subsamples causes r_c to behave this way. In §5.2 we showed that while Sample-D consists of systems with well-behaved velocity dispersion profiles, most other systems have profiles which are inconsistent. Therefore the conclusions drawn from Sample-D are more robust than those drawn from the high- and low- σ_p subsamples.
5. The fits support the results of our statistical tests in §6. For all our subsamples, the best-fit r_c is smaller for the absorption- than for the emission-dominated galaxies; the two-dimensional 68.4% confidence contours never overlap.

7.2. Velocity Dispersion Profiles

The three-dimensional radial velocity dispersion $\overline{v_r^2}$ for a spherical, nonrotating system is given by the Jeans equation (Binney & Tremaine 1987):

$$\frac{1}{\rho} \frac{d}{dr} (\rho \overline{v_r^2}) + 2\beta \frac{\overline{v_r^2}}{r} = -\frac{GM(r)}{r^2}; \quad (14)$$

where $\tilde{r} = r/r_c$ and $\beta = 1 - \overline{v_\theta^2}/\overline{v_r^2}$ is the velocity anisotropy parameter. We solve the Jeans equation for the Hernquist (1990) profile, where

$$M(r) = \frac{4M_c \tilde{r}^2}{(\tilde{r} + 1)^2}. \quad (15)$$

The Hernquist (1990) density profile yields a much simpler expression for $\overline{v_r^2}$ than does NFW model; because both models fit our spatial data well, we only consider the former. In solving the equation we use constant β , rather than assuming some functional form $\beta(r)$ from N-body simulations as Carlberg et al. (1997b) do. Because we are not dealing with rich clusters in this work, we would like freedom from the assumptions that the β profiles from simulations of clusters necessitate, e.g., that the velocity dispersion is isotropic near the core ($\beta = 0$) and that β achieves a maximum somewhere beyond the virial radius (Cole & Lacey 1996; Diaferio 1999). We therefore seek to establish the average value of β for our systems.

For constant β and the Hernquist (1990) profile, equation (14) has the solution,

$$\overline{v_r^2} = -\frac{4GM_c}{r_c} \frac{(\tilde{r} + 1)^3}{\tilde{r}^{2\beta-1}} \int \frac{\tilde{r}^{2\beta-1}}{(\tilde{r} + 1)^5} d\tilde{r}. \quad (16)$$

While there is no analytic form for the above integral when β is a real number, it is possible to represent the solution as the following series (see §E),

$$\overline{v_r^2} = \frac{GM_c}{r_c} \tilde{v}(\tilde{r})^2, \quad (17)$$

$$\tilde{v}(\tilde{r})^2 = \frac{4\tilde{r}}{(5 - 2\beta)(\tilde{r} + 1)^2} \sum_{i=0}^{\infty} C_i (\tilde{r} + 1)^{-i}, \quad (18)$$

$$C_i = \prod_{j=1}^i \frac{5 + j - 1}{5 + j - 2\beta}, \quad (19)$$

where $C_0 \equiv 1$. Note that we have set the integration constant equal to zero to suppress divergent solutions as $\tilde{r} \rightarrow \infty$. Equations 17–19 imply $\lim_{r \rightarrow 0} \overline{v_r^2} = \infty$ when $\beta > 0.5$, $\lim_{r \rightarrow 0} \overline{v_r^2} = GM_c/r_c$ when $\beta = 0.5$, and $\lim_{r \rightarrow 0} \overline{v_r^2} = 0$ when $\beta < 0.5$. The series always

converges for $r > 0$, because $\beta \leq 1$; it converges rapidly when either $\beta < 0.5$ or $\tilde{r} > 1$, and slowly when both $\beta \geq 0.5$ and $\tilde{r} < 1$. In computing the series we use double precision numbers to minimize roundoff error, and add terms until we achieve a fractional accuracy of 10^{-6} . For the worst convergence case ($r \approx 0$, $\beta = 1$) we check the above series formula with the analytic solution

$$\overline{v_r^2} = \frac{GM_c}{r_c} \frac{1 + 4\tilde{r}}{3\tilde{r}(\tilde{r} + 1)}. \quad (20)$$

For this worst-case scenario, the series and the analytic solution produce identical results to 3 decimal places for $\tilde{r} = 0.001$ (which in practice never enters into consideration), and to 5 decimal places when $\tilde{r} \geq 0.01$.

The projected velocity dispersion profile is (Binney & Tremaine 1987)

$$\sigma_p^2(R) = \frac{2N_c}{M_c \Sigma(R)} \int_R^\infty \left(1 - \beta \frac{R^2}{r^2}\right) \frac{\rho \overline{v_r^2} r dr}{\sqrt{r^2 - R^2}}. \quad (21)$$

which we evaluate numerically by reformulating as

$$\sigma_p^2(\tilde{R}) = \frac{4GM_c N_c}{\pi r_c^3 \Sigma(\tilde{R})} \int_0^{1/\tilde{R}} \left(1 - \beta \tilde{R}^2 t^2\right) \frac{\tilde{v}(1/t)^2 t^2 dt}{(t+1)^3 \sqrt{1 - \tilde{R}^2 t^2}}. \quad (22)$$

We integrate the inverse-square-root singularity by using the extended midpoint rule techniques described in Press et al. (1992; §4.4), which we modify to work with double-precision numbers. Note that once we specify r_c from fits to the spatial data, the only free parameters in the theoretical $\sigma_p(R)$ are β and M_c .

The combined projected velocity dispersion profiles for the low- and high- σ_p subsamples are too irregular to be good fits to simple density models. We fit only the combined profile for the well-behaved set of systems with declining $\sigma_p(R)$ (Sample-D, described in §6). We fix r_c at the value obtained from the spatial data, and fit β and $GM_c/(r_c \sigma_p^2)$ as our two free parameters. The total mass of the Hernquist (1990) model results directly from our fit; $M_{\text{tot}} = 4M_c$.

Figures 18-19 show the results of the fits, which have $\chi^2/\nu < 1$ for both the emission- and absorption-dominated samples taken either individually or together. Therefore, a Hernquist (1990) profile, with a core radius taken from spatial data, fits the velocity data well, suggesting that Sample-D is well described by a spherically symmetric model with a simple velocity distribution function.

It is perhaps more remarkable that the systems which have non-falling $\sigma_p(R)$ are still well fit by the simple Hernquist (1990) and NFW surface density distributions. Our data suggest that while a spherically symmetric mass distribution provides a good representation

of all our systems, the orbital families are irregularly populated, and $\beta(r, \theta, \phi)$ has a complicated behavior; it may not be represented as a spherically symmetric function even though the mass density is. This, in turn, is further evidence that our systems, with the exclusion of Sample-D, may not be in dynamical equilibrium.

Because the best-fit $\beta > 0$ for both absorption- and emission-dominated members in Sample-D, both sets of galaxies are probably dominated by radial orbits. The one-dimensional 95.4% confidence contour for the emission-dominated galaxies never extends below $\beta = 0.2$; we can therefore rule out orbital isotropy for them at that level. On the other hand, the orbits of the absorption-dominated galaxies are consistent with isotropy at the same level.

Finally, we compute the masses traced by the galaxies. For Sample-D as a whole, the 68.3% confidence interval on the total mass, not considering systematic effects, is

$$M_{\text{tot}} = (1.2 \pm 0.2)h^{-1} \times 10^{14} M_{\odot} \left(\frac{\sigma_p}{300 \text{ km s}^{-1}} \right)^2. \quad (23)$$

The separate fits to the absorption- and emission-dominated galaxies yield

$$M_{\text{tot}}^a = (1.0 \pm 0.2)h^{-1} \times 10^{14} M_{\odot} \left(\frac{\sigma_p}{300 \text{ km s}^{-1}} \right)^2; \quad (24)$$

$$M_{\text{tot}}^m = (2.0 \pm 0.5)h^{-1} \times 10^{14} M_{\odot} \left(\frac{\sigma_p}{300 \text{ km s}^{-1}} \right)^2; \quad (25)$$

$$\frac{M_{\text{tot}}^m}{M_{\text{tot}}^a} = 2.0 \pm 0.6. \quad (26)$$

The absorption-dominated galaxies trace a mass that is entirely consistent with Sample-D as a whole. The emission-dominated members apparently trace a larger mass. The discrepancy in the mass estimates may be due to fitting $\sigma_p(R)$ for a combined sample rather than on a case-by-case basis. It is also likely that equilibrium models do not provide an entirely appropriate description of the emission-dominated members. If the star-forming galaxies are on predominantly radial orbits, and are falling in for the first time as suggested by our timing arguments (§5.2), they probably have not reached dynamical equilibrium, and are not as well described by the Jeans equations as the absorption-dominated members.

8. Conclusions

We analyze a sample of 20 galaxy systems drawn from a larger, objectively selected catalog of systems in the Center for Astrophysics redshift survey. Each system has a membership complete to $m_R \approx 15.4$ out to a projected radius $1.5h^{-1}$ Mpc from its center.

1. Most of the systems have significantly more members after our observations than they had in the original source catalog (Ramella et al. 1997). Of the 12 systems with statistically significant, extended x-ray emission, 11 more than tripled their original membership. We conclude that our x-ray emitting systems have a high likelihood of being real, bound groups or clusters. Of the 8 objects without significant extended emission, one (NRGb043) quintupled its membership, and may have x-ray emission below the detection threshold of the ROSAT All Sky Survey; some of the other systems are unlikely to be bound configurations.
2. We use fits to template optical spectra, along with the two-dimensional KS Test (§C), to classify the galaxies we observe into absorption- and emission-line dominated populations. We find evidence of spectroscopic segregation: the members with active star formation have consistently larger mean distances from the system center than the members with older stellar populations. Most systems have many more absorption- than emission-dominated galaxies in the projected regions encompassed by the x-ray emission contours.
3. The line-of-sight velocity dispersion as a function of projected radius, $\sigma_p(R)$, is a useful tool for testing whether our systems are in similar dynamical states. A quarter of the sample exhibits declining velocity dispersion profiles similar to the those implied by N-body simulations (Crone et al. 1994; Navarro, Frenk, & White 1997). The remaining 75% of the systems exhibit flat, rising and irregularly varying profiles. The null hypothesis that $\sigma_p(R)$ is drawn from the same distribution is rejected with better than 99% significance for 41% of all unique pairs of systems.
4. Both the Hernquist model (1990) and the Navarro, Frenk, & White (1997; NFW) universal profile provide good fits to the spatial data, assuming that galaxies in our sample trace the system mass uniformly. The isothermal sphere is usually ruled out. Our best-behaved subsample (with intermediate velocity dispersions, $\sigma_p = 327\text{--}466$ km s $^{-1}$) yields a NFW concentration $c = 4.3\text{--}9.1$ (95.4% confidence interval). This is slightly larger than the range for rich clusters (Carlberg et al. 1997a,b), 2.3–7.7, and therefore consistent with NFW’s prediction that the concentration should decrease as the mass increases.

5. We solve the Jeans equation for the Hernquist (1990) profile using a constant velocity anisotropy parameter β ; we project the solution numerically, and fit the theoretical $\sigma_p(R)$ to the best-behaved subsample. The theoretical profile provides a good fit, and the one-dimensional 95.4% confidence interval for β allows only predominantly radial orbits ($\beta > 0$) for galaxies with active star formation. Galaxies with older stellar populations have orbits which are consistent with isotropy to within the errors. The star-forming galaxies with predominantly radial orbits, especially those at a distance of $\approx 1.5h^{-1}$ Mpc, probably have not made many crossings of the system diameter, since they move only $2h^{-1}$ – $4h^{-1}$ Mpc in a Hubble time. Many of them may be falling in for the first time.
6. Remarkably, the systems with irregular or rising velocity dispersion profiles have a spatial structure which is well-described by the Navarro, Frenk, & White (1997) and the Hernquist (1990) density profiles. Because these systems have surface number densities which are well-described by theoretical collapsed-halo profiles, but have velocity structure which no simple model can fit, they are probably bound configurations which are not in dynamical equilibrium.

In future articles we plan a detailed spectroscopic analysis of individual system members to measure star formation rates, find galaxies which show evidence of truncated star formation, and model the relationship between the spectroscopic properties and the shape of the x-ray emitting region in our systems.

Thanks are due to the remote observers on the 60" Tillinghast Reflector, Perry Berlind, and Michael Calkins, who together measured many of the spectra for this work. We remember Jim Peters, who made more than a fourth of the observations, with fondness; *sic itur ad astra*. Brian McLean graciously provided positions for the galaxies within $28 \leq \delta_{2000} \leq 32$. We could not have done without Susan Tokarz, who did the preliminary reductions of the data. We thank Gregory Bothun and Ben Moore for comments which improved the paper.

This project is based on photographic data of the National Geographic Society – Palomar Observatory Sky Atlas (POSS-I) made by the California Institute of Technology. The plates were processed into the present compressed digital form with their permission. The Digitized Sky Survey was produced at the Space Telescope Science Institute under US Government grant NAG W-2166. A. Mahdavi, M. J. Geller, and M. J. Kurtz acknowledge support from the Smithsonian Institution; A. Mahdavi also acknowledges a National Science Foundation Graduate Student Fellowship. M. Ramella acknowledges support from the Italian Space Agency and from the Italian National Research Council.

Appendices

A. Definitions

We use “system” to describe any set of galaxies which an objective structure-finding method places together as a unit. A system is “bound” if it is self-gravitating; it is an “artifact” if the objective method mistakenly placed physically unrelated galaxies together. The “membership” of a system is the set of all galaxies that have negative total gravitational energy in the center of mass frame; all other galaxies assigned to the system are “interlopers.”

A system with N members, each with a measured redshift z_i and accompanying Gaussian uncertainty Δz_i , has a recession velocity $\langle v \rangle$, traditionally estimated by $\bar{v} \equiv \sum_i cz_i/N$, where c is the speed of light. The i th member has a peculiar line-of-sight velocity $v_i \equiv (cz_i - \langle v \rangle) / (1 + \langle v \rangle/c)$. The global projected velocity dispersion of the system is σ_p , where traditionally σ_p^2 is estimated by $\text{Var}(v) \equiv \sum_i (v_i - \langle v \rangle)^2 / (N - 1)$. The standard deviation is defined as $\sqrt{\text{Var}(v)}$. In §D we consider robust estimators of $\langle v \rangle$ and σ_p .

We indicate three-dimensional distances from the system center with a lowercase r , while reserving the uppercase R for projected distance on the sky. In our article the “field” of a system is a circle on the sky with the same center as the system, and with radius $\theta \equiv 150 \text{ km s}^{-1} / \langle v \rangle$. In other words, the field is always large enough to include a $R = 1.5h^{-1} \text{ Mpc}$ region around the system center.

B. On Bootstraps With Measurement Errors

When the probability distribution underlying the data, $D(x)$, is *a priori* unknown—as is the case with the velocity distribution of system members—it is not possible to compute confidence intervals analytically for some parameter, a , derived from the data. The bootstrap is a numerical method for obtaining these confidence intervals by using the data set itself as an estimate of the underlying distribution (see, e.g., Lupton 1993). Classically, for a data set x_i of length N ,

$$D(x) \equiv \frac{1}{N} \sum_i^N \delta(x - x_i) \quad (\text{B1})$$

Here $\delta(x)$ is the Dirac delta function. To compute the confidence interval on a , one usually draws a large number of data sets of length N from $D(x)$, and by recomputing a each time, derives its probability distribution. For the case that $D(x)$ is a sum of delta functions, this procedure is tantamount to selecting points from the data set with replacement.

Unfortunately, by representing each data point as a delta function, $D(x)$ neglects the uncertainty accompanying that measurement. The probability distribution of each individual measurement is not $\delta(x - x_i)$, but some error distribution $E(x)$ centered on the measurement. In the case of our redshift measurements, $E(z)$ is a Gaussian with a standard deviation $\Delta z_i \approx 10^{-4}$. Therefore the correct bootstrap data probability distribution is

$$D(z) \equiv \frac{1}{\sqrt{2\pi}N} \sum_i^N \frac{1}{\Delta z_i} \exp \left[-\frac{(z - z_i)^2}{\Delta z_i^2} \right] \quad (\text{B2})$$

Drawing deviates distributed as $D(z)$ is a bit more tricky than selecting with replacement, as is possible with the delta function distribution. We use a rejection method, as outlined for example in Press et al. (1992, §7.3), with a constant comparison function over the range of the data. All the bootstrap confidence intervals for the parameters we derive therefore take the measurement uncertainties into account properly.

Note that $D(x)$, $D(z)$ and the adaptive kernel estimator f_{ka} , defined in equation (1), are only superficially related. The first two are minimal representations of the distribution of the data, constructed for the purpose of deriving alternate data sets drawn from a similar parent population. The adaptive kernel, on the other hand, attempts to overcome the effects of sampling as it builds its guess at the true shape of the parent distribution.

C. On the Two-Dimensional KS Test

The Kolmogorov-Smirnov Test (e.g., Press et al. 1992, §14.3) evaluates the null hypothesis that a pair of data sets are drawn from the same distribution. In the simple case that each data set is one dimensional, the corresponding KS Test (KS1D) computes d_1 , the maximum deviation of the two data cumulative distributions. The *a priori* distribution of d_1 itself is known, and therefore so is the probability of the null hypothesis. The KS1D test is particularly useful, because its estimate of the probability is independent of the original distributions of the data, which are often not known.

We use a version of the Kolmogorov-Smirnov test (KS2D; e.g. Press et al. 1992, §14.7) which is applicable to two-dimensional data sets. Because the notion of a cumulative distribution is poorly defined for a two-dimensional data set, the corresponding deviation statistic, d_2 , is calculated somewhat differently. Suppose we are comparing two data sets, (x_i, y_i) , $i = 1 \dots N_1$ and (X_j, Y_j) , $j = 1 \dots N_2$. For each (x_i, y_i) compute

$$\mathcal{D}_i \equiv \max \left(\left| \sum_{x < x_i, y < y_i} \frac{1}{N_1} - \sum_{X < x_i, Y < y_i} \frac{1}{N_2} \right|, \left| \sum_{x > x_i, y < y_i} \frac{1}{N_1} - \sum_{X > x_i, Y < y_i} \frac{1}{N_2} \right| \right),$$

$$\left| \sum_{x < x_i, y > y_i} \frac{1}{N_1} - \sum_{X < x_i, Y > y_i} \frac{1}{N_2} \right|, \left| \sum_{x > x_i, y > y_i} \frac{1}{N_1} - \sum_{X > x_i, Y > y_i} \frac{1}{N_2} \right| \Bigg). \quad (\text{C1})$$

Define \mathcal{D}_j similarly, replacing i with j , x_i with X_j , and y_i and Y_j in the above equation. Then

$$d_2 \equiv \left(\frac{N_1 N_2}{N_1 + N_2} \right)^{\frac{1}{2}} \times \frac{\max(\mathcal{D}_i) + \max(\mathcal{D}_j)}{2} \quad (\text{C2})$$

To compute d_2 we use the computer code which Press et al. (1992) implement on the basis of theoretical work by Fasano & Franceschini (1987). However, we do not use the Press et al. (1992) prescription to compute the probability of the null hypothesis, because it is only accurate for $N \gtrsim 20$ data points. Rather we use the results of Fasano & Franceschini (1987) directly; they fit a third-order polynomial in three variables (sample size, sample correlation, and desired significance level) to their Monte Carlo simulations of the probability distribution of d_2 . They find that the fractional uncertainty of the resultant probabilities for the null hypothesis is $\sim 5\%$.

Note that the output d_P of the Press et al. (1992) computer program is normalized differently from our notation for d_2 , which agrees with that of Fasano & Franceschini (1987):

$$d_2 = d_P \left(\frac{N_1 N_2}{N_1 + N_2} \right)^{\frac{1}{2}}. \quad (\text{C3})$$

D. Comparison of the Robust and Classical Estimators of the Velocity Moments

The classical estimators of the system recession velocity $\langle v \rangle$ and the line-of-sight velocity dispersion σ_p are the mean velocity \bar{v} and the unbiased standard deviation estimator $\sqrt{\text{Var}(v)}$, respectively (see §A). However, Beers, Flynn, & Gebhardt (BFG; 1990) argue that the sample mean and the sample standard deviation are not, in general, efficient estimators of the properties of a parent distribution $p(x)$. For example, if $p(x)$ is not a Gaussian, \bar{x} is in general a poorer estimator of $\langle x \rangle$, and $\text{Var}(x)$ is a poorer estimator $\langle (x - \langle x \rangle)^2 \rangle$, than certain robust estimators which we compute alongside the classical estimators.

In Figure 20 we show \bar{v} alongside the sample median M , and the biweight location estimator,

$$\text{BiMean} = M + \frac{\sum_{|\mu_i| < 1} (cz_i - M) (1 - \mu_i^2)^2}{\sum_{|\mu_i| < 1} (1 - \mu_i^2)}; \quad (\text{D1})$$

$$\mu_i = \frac{(x_i - M)}{c \times \text{MAD}}; \quad (\text{D2})$$

$$\text{MAD} = \text{median}(|x_i - M|). \quad (\text{D3})$$

Here c is an arbitrary tuning parameter. Similarly, we list the standard deviation alongside the “Gapper,” which uses the weighted gaps among the data points to compute the scale of the velocity distribution (see BFG for its definition); we also show the biweight scale estimator,

$$\text{BiSigma} = n^{1/2} \frac{\left[\sum_{|\mu_i| < 1} (cz_i - M) (1 - \mu_i^2)^4 \right]^{1/2}}{\left| \sum_{|\mu_i| < 1} (1 - \mu_i^2) (1 - 5\mu_i^2) \right|} \quad (\text{D4})$$

Interestingly, these various estimators differ very little (Figure 20). For all systems, the robust biweight estimates of the recession velocity and velocity dispersion lie well within the 68.3% confidence interval of the classical estimators, the mean and the standard deviation. The median, which is not efficient in the presence of substructure (BFG), lies outside the confidence interval of the mean only twice. The even closer agreement of the estimators of σ_p , a quantity somewhat more important for kinematic analysis than $\langle v \rangle$, is also noteworthy.

In considering which of the two kinds of estimators, classical or robust, we should use, we note that the latter make use of a dimensionless tuning constant c , which BFG set to 6.0 for the biweight location estimator, and to 9.0 for the scale estimator. The biweights also require the subjective choice of an auxiliary estimator of scale; BFG use the mean absolute deviation (“MAD”). On the other hand the classical estimators contain no arbitrary parameters.

We therefore adopt $\langle v \rangle = \bar{v}$ and $\sigma_p = \sqrt{\text{Var}(v)}$. All the quoted errors on the velocity moments are 68.3% bias-corrected bootstrap confidence intervals as described in §B.

E. Integration of Constant- β Jeans Equation

Equation (16) is integrable through the identity,

$$\int x^m (a + bx)^n dx = \frac{x^{m+1} (a + bx)^n}{m + n + 1} + \frac{an}{m + n + 1} \int x^m (a + bx)^{n-1} dx. \quad (\text{E1})$$

Substituting $a = b = 1$, $x = \tilde{r}$, $m = 2\beta - 1$, and $n = -5$, and applying the above expression to the integral in equation 16, we obtain

$$\int \frac{\tilde{r}^{2\beta-1}}{(\tilde{r} + 1)^5} d\tilde{r} = \frac{1}{2\beta - 5} \left\{ \frac{\tilde{r}^{2\beta}}{(\tilde{r} + 1)^5} - \frac{5}{2\beta - 6} \left[\frac{\tilde{r}^{2\beta}}{(\tilde{r} + 1)^6} - \frac{6}{2\beta - 7} \left(\frac{\tilde{r}^{2\beta}}{(\tilde{r} + 1)^7} - \dots \right) \right] \right\} \quad (\text{E2})$$

$$= -\frac{\tilde{r}^{2\beta}}{(\tilde{r}+1)^5} \frac{1}{5-2\beta} \left\{ 1 + \frac{5}{6-2\beta} \left[\frac{1}{(\tilde{r}+1)} + \frac{6}{7-2\beta} \left(\frac{1}{(\tilde{r}+1)^2} + \dots \right) \right] \right\} \quad (23)$$

From the above relation, equations 17–19 follow easily.

References

- Abell, G. O. 1958, *ApJS*, 3, 211
- Albert, C. E., White, R. A., & Morgan, W. W. 1977, *ApJ*, 211, 309
- Anderson, S. 1996, *A&A*, 314, 763
- Antonuccio-Delogu, V., & Colafrancesco, S. 1994, *ApJ*, 427, 72
- Athanassoula, E., Makino, J., & Bosma, A. 1997, *MNRAS*, 286, 825
- Barton, E., de Carvalho, R. R., & Geller, M. J. 1998, *AJ*, in press
- Beers, T. C., Flynn, K., & Gebhardt, K. 1990, *AJ*, 100, 32
- Binney, J., and Tremaine, S. 1987, *Galactic Dynamics* (Princeton: Princeton University Press)
- Bode, P. W., Cohn, H. N., & Lugger, P. M. 1993, *ApJ*, 416, 17
- Bode, P. W., Berrington, R. C., Cohn, H. N., & Lugger, P. M. 1994, *ApJ*, 433, 479
- Boller, T., Bertoldi, F., Dennefeld, M., & Voges, W. 1998, *A&AS*, 129, 87
- Carlberg, R. G., Yee, H. K. C., Ellingson, E., Morris, S. L., Abraham, R., Gravel, P., Pritchet, C. J., Smecker-Hane, T., Hartwick, F. D. A., Hessler, J. E., Hutchings, J. B., & Oke, J. B. 1997a, *ApJ*, 476, L7
- Carlberg, R. G., Yee, H. K. C., Ellingson, E., Morris, S. L., Abraham, R., Gravel, P., Pritchet, C. J., Smecker-Hane, T., Hartwick, F. D. A., Hessler, J. E., Hutchings, J. B., & Oke, J. B. 1997b, *ApJ*, 495, L13
- Cole, S., & Lacey, C. G. 1996, *MNRAS*, 281, 716
- Colless, M., & Dunn, A. M. 1996, *ApJ*, 458, 435
- Crone, M. M., Evrard, A. E., & Richstone, D. O. 1994, *ApJ*, 434, 402
- Da Costa, L. N., Geller, M. J., Pellegrini, P. S., Latham, D. W., Fairall, A. P., Marzke, R. O., Willmer, C. N. A., Huchra, J. P., Calderon, J. H., Ramella, M., and Kurtz, M. J. 1994, *ApJ*, 424, L1
- Da Costa, L. N., Willmer, C. N. A., Pellegrini, P. S., Chaves, O. L., Maia, M. A. G., Geller, M. J., Latham, D. W., Kurtz, M. J., Huchra, J. P., Ramella, M., Fairall, A. P., Smith, C., & Lipari, S. 1998, *AJ*, 116, 1

- Dell’ Antonio, I. P., Geller, M. J., & Fabricant, D. G. 1994, *AJ*, 107, 427
- Diaferio, A., Ramella, M., Geller, M. J., Ferrari, A. 1993, *AJ*, 105, 2035
- Diaferio, A., Geller, M. J., & Ramella, M. 1994, *AJ*, 107, 868
- Diaferio, A., Kauffmann G., Colberg, J. M., and White, S. D. M. 1999, submitted to *MNRAS*
- Diaferio, A. 1999, submitted to *ApJ*
- Dressler, A. 1980, *ApJ*, 236, 351
- Dressler, A., & Shectman, S. A. 1998, *AJ*, 95, 985
- Fabricant, D., Cheimets, P., Caldwell, N., and Geary, J. 1998, *PASP*, 110, 79
- Falco, E. E., Kurtz, M. J., Geller, M. J., Huchra, J. P., Peters, J., Berlind, P., Mink, D. J., Tokarz, S. P., and Elwell, B. 1999, *PASP*, in press
- Fasano, G., & Franceschini, A. 1987, *MNRAS*, 225, 155
- Frederic, J. 1995a, *ApJS*, 97, 259
- Frederic, J. 1995b, *ApJS*, 97, 275
- Frei, Z., & Gunn, J. E., 1994, *AJ*, 111, 174
- Geller, M. J., & Huchra, J. P. 1989, *Science*, 246, 897
- Girardi, M., Fadda, D., Guiricin, G., Mardirossian, F., Mezzetti, M., & Biviano, A. 1996, *ApJ*, 457, 61
- Gourgoulhon, E., Chamaraux, P., & Fouque, P. 1992, *A&A*, 255, 69
- Hernquist, L. 1990, *ApJ*, 356, 359
- Hernquist, L., Katz, N., & Weinberg, D. H. 1995, *ApJ*, 442, 57
- Hickson, P. 1982, *ApJ*, 255, 382
- Huchra, J. P., & Geller, M. J. 1982, *ApJ*, 257, 423
- Huchra, J. P., de Lapparent, V., Geller, M. J., & Corwin, Jr., H. G. 1990, *ApJS*, 72, 433
- Huchra, J. P., Geller, M. J., & Corwin, Jr., H. G. 1995, *ApJS*, 70, 687
- Kurtz, M. J., Mink, D. J., Wyatt, W. F., Fabricant, D. G., Torres, G., Kriss, G. A., and Tonry, J. L. 1992, in *Astronomical Data Analysis Software and Systems I*, A. S. P.

- conference series, Vol. 25, Worrall, D. M., Biemesderfer, C., and Barnes, J., eds., p. 432
- Kurtz, M. J., & Mink, D. J. 1998, *PASP*, 110, 934
- Lahav, O., & Saslaw, W. C. 1992, *ApJ*, 396, 430
- Lupton, R. 1993, *Statistics in Theory and Practice* (Princeton: Princeton University Press)
- Mahdavi, A., Geller, M. J., Fabricant, D. G., Kurtz, M. J., Postman, M., and McLean, B. 1996, *AJ*, 111, 64
- Mahdavi, A., Böhringer, H., Geller, M. J., & Ramella, M. 1997, *ApJ*, 483, 68
- Mahdavi, A., Böhringer, H., Geller, M. J., & Ramella, M. 1999, in preparation
- Marzke, R. O., Huchra, J. P., & Geller, M. J. 1993, *ApJ*, 428, 43
- Menci, N., & Fusco-Femiano, R. 1996, *ApJ*, 472, 46
- Mohr, J. J., Geller, M. J., Fabricant, D. G., Wegner, G., Thorstensen, J., & Richstone, D. O. 1996, *ApJ*, 470, 724
- Moore, B., Frenk, C. S., & White S. D. M. 1993, *MNRAS*, 261, 827
- Kurtz, M. J., & Mink, D. J. 1998, *PASP*, in press
- Morgan, C. G., & Hartwick, F. D. A. 1988, *ApJ*, 328, 381
- Mulchaey, J. S., & Zabludoff, A. I. 1998, *ApJ*, 496, 73
- Navarro, J. F., Frenk. C. S., & White, S. D. M. 1997, *ApJ*, 490, 493
- Nolthenius, R., Klypin, A. A., & Primack, J. R. 1994, *ApJ*, 422, L45
- Nolthenius, R., Klypin, A. A., & Primack, J. R. 1997, *ApJ*, 480, 43
- Ostriker, J. P., Lubin, L. M., & Hernquist, L. 1995, *ApJ*, 444, L61
- Pedersen, K., Yoshi, Y., & Sommer-Larsen, J. 1997, *ApJ*, 485, L17
- Persic, M., & Salucci, P. 1992, *MNRAS*, 258, 14
- Pisani, A. 1993, *MNRAS*, 265, 706
- Pisani, A. 1996, *MNRAS*, 278, 697
- Ponman, T. J., Bourner, P. D. J., Ebeling, H., & Böhringer, H. 1996, *MNRAS*, 283, 690
- Postman, M., Geller, M. J. 1984, *ApJ*, 281, 95

- Press, W. H., Teukolsky, S. A., Vetterling, W. T., and Flannery, B. P. 1992, *Numerical Recipes in C*, Second Edition (Cambridge, England: Cambridge University Press)
- Ramella, M., Geller, M. J., & Huchra, J. P. 1989, *ApJ*, 344, 57
- Ramella, M., Geller, M. J., Huchra, J. P., & Thorstensen, H. R., 1995, *AJ*, 109, 1458 (RGHT)
- Ramella, M., Pisani, A., & Geller, M. J. 1997, *AJ*, 113, 483 (RPG)
- Ramella, M., et al. 1999, in preparation
- Shapley, H. 1933, *Proc. Nat. Acad. Sci.* 19, 591
- Schechter, P. 1976, *ApJ*, 203, 297
- Schwartz, D. A., Schwarz, J., and Tucker, W. 1980, *ApJ*, 238, L59
- Stein, P. 1997, *A&A*, 317, 670
- Tonry, J. L., & Davis, M. 1979, *AJ*, 84, 1511
- Trasarti-Battistoni, R. 1998, *A&AS*, 130, 341
- Valdes, F. 1992, in *Astronomical Data Analysis Software and Systems*, A. S. P. conference series, Vol. 25, Worrall, D. M., Biemesderfer, C., and Barnes, J., eds., p. 417
- Valdes, F. G., Campusano, L. E., Velasquez, J. D., & Stetson, P. B. 1995, *PASP*, 107, 1119
- Vio, R., Fasano, G., Lazzarin, M., and Lessi, O. 1994, *A&A*, 289, 640
- Voges, W. 1993, *Advances in Space Research*, 13, (12)391
- Walke, D. G., & Mamon, G. A. 1989, *A&A*, 225, 291
- Whitmore, B. C., Gilmore, D. M., & Jones, C. 1993, *ApJ*, 407, 489
- Zabludoff, A. I., & Mulchaey, J. S. 1998, *ApJ*, 496, 39
- Zwicky, F., & Humason, M. L. 1960, *ApJ*, 132, 627

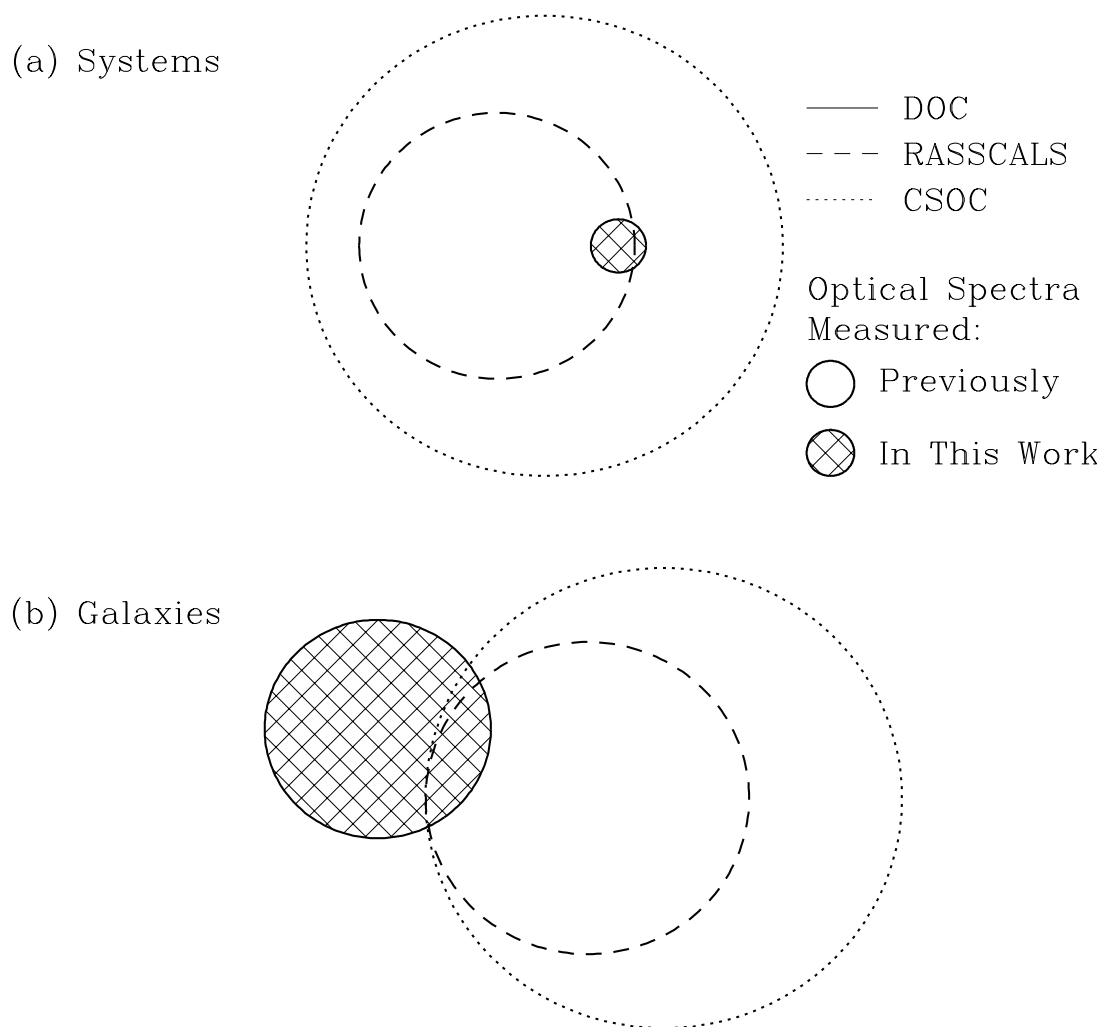


Fig. 1.— Venn diagrams showing the relationship among the Deep Optical Catalog (This paper), the RASSCALs (Mahdavi et al. 1999), and the CfA-SSRS2 Optical Catalog (Ramella et al. 1999). In (a), the circles represent the set of all galaxy systems in each catalog. The area of each circle is proportional to the number of systems it contains; the areas of the intersections accurately represent the degree of overlap among the catalogs. In (b), the circles represent the set of all galaxies classified as system members in each catalog. The area of each circle is proportional to the total number of galaxies classified as members, and the areas of the intersections accurately reflect the number of galaxies the catalogs share.

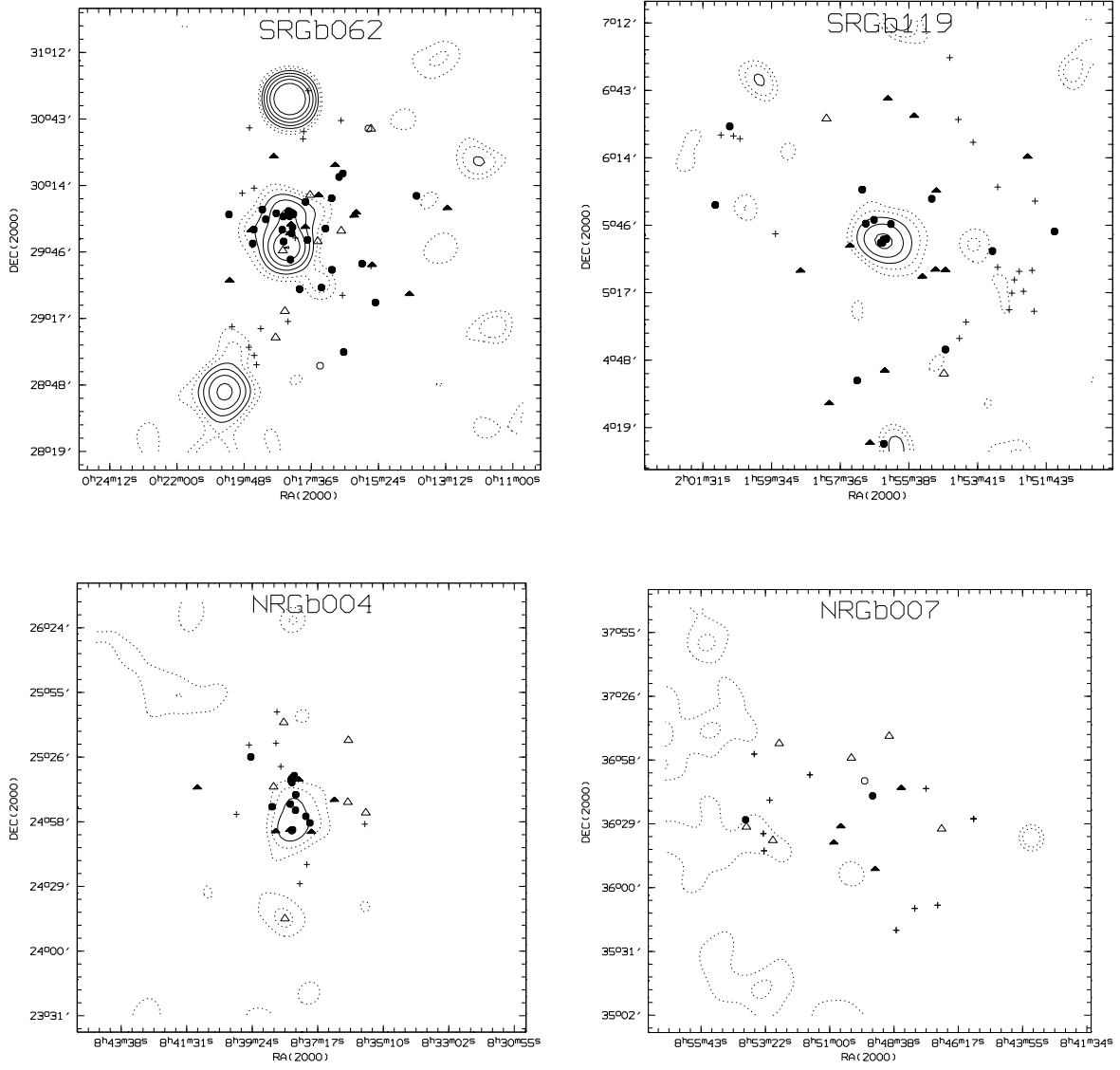


Fig. 2.— Galaxy positions and x-ray contours. The x-ray emission contours begin at 1.33 standard deviations above the level of the background, and increase by a factor of 1.5; dotted contours lie less than 3.0 standard deviations above the background. Galaxies with $cz > 15000 \text{ km s}^{-1}$ are simply shown as crosses; they are never system members. Galaxies with $500 \text{ km s}^{-1} \leq cz \leq 15000 \text{ km s}^{-1}$ are marked by circles if their spectra are absorption dominated, or by triangles if the spectra are emission-dominated. Each triangle or circle is filled-in if the galaxy is a system member, empty if it is not.

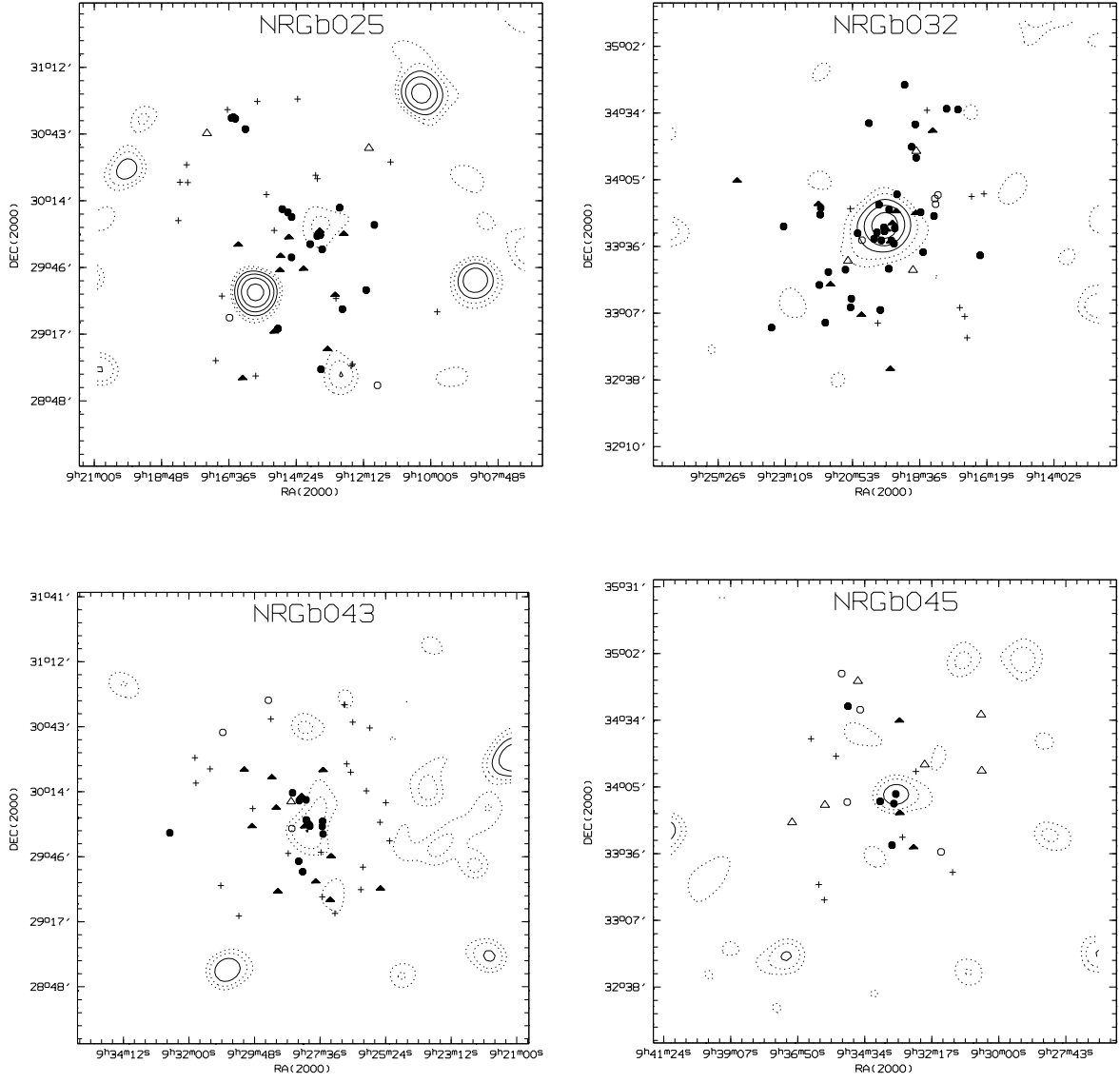


Fig. 3.— See caption for Figure 2.

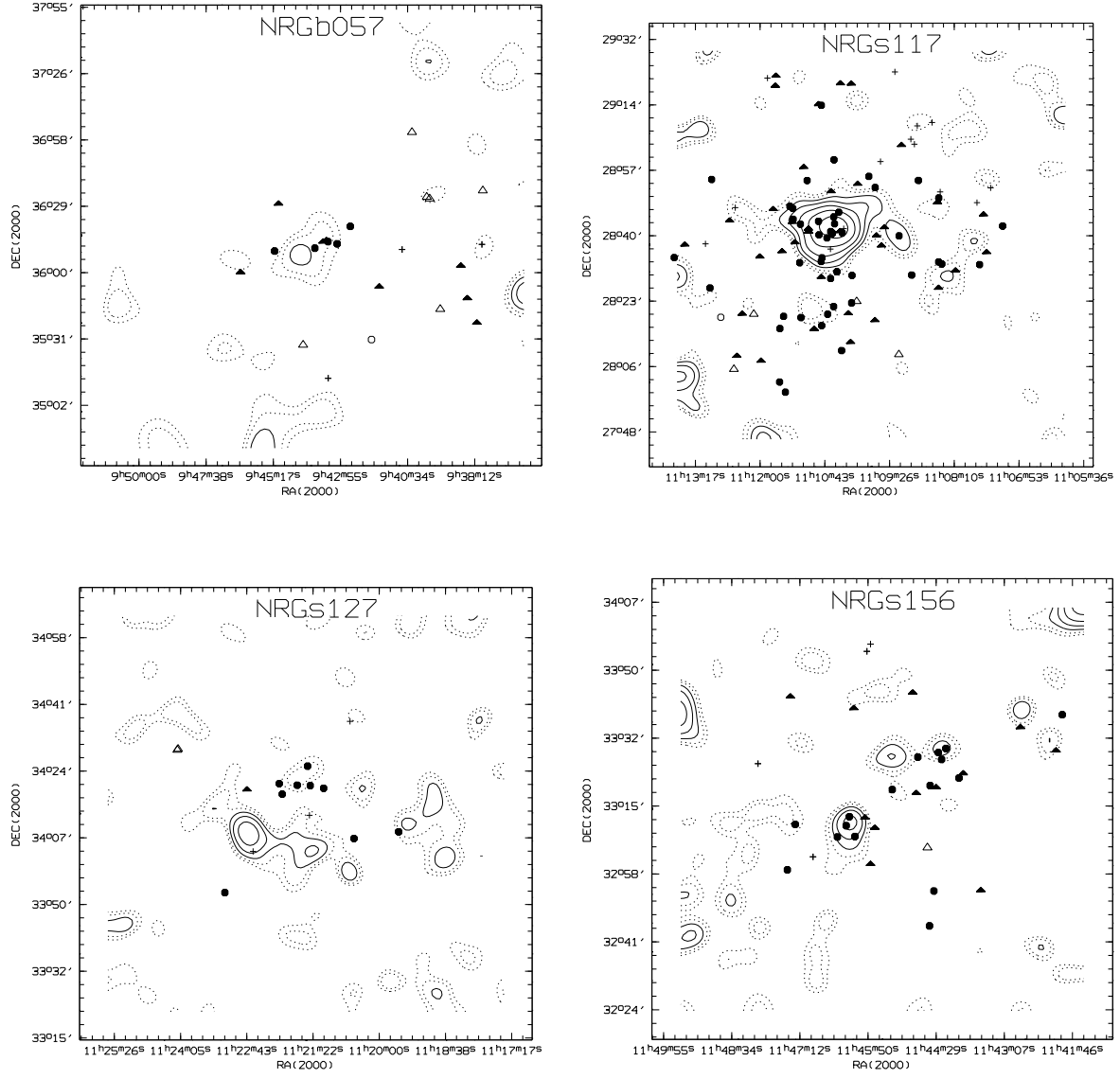


Fig. 4.— See caption for Figure 2.

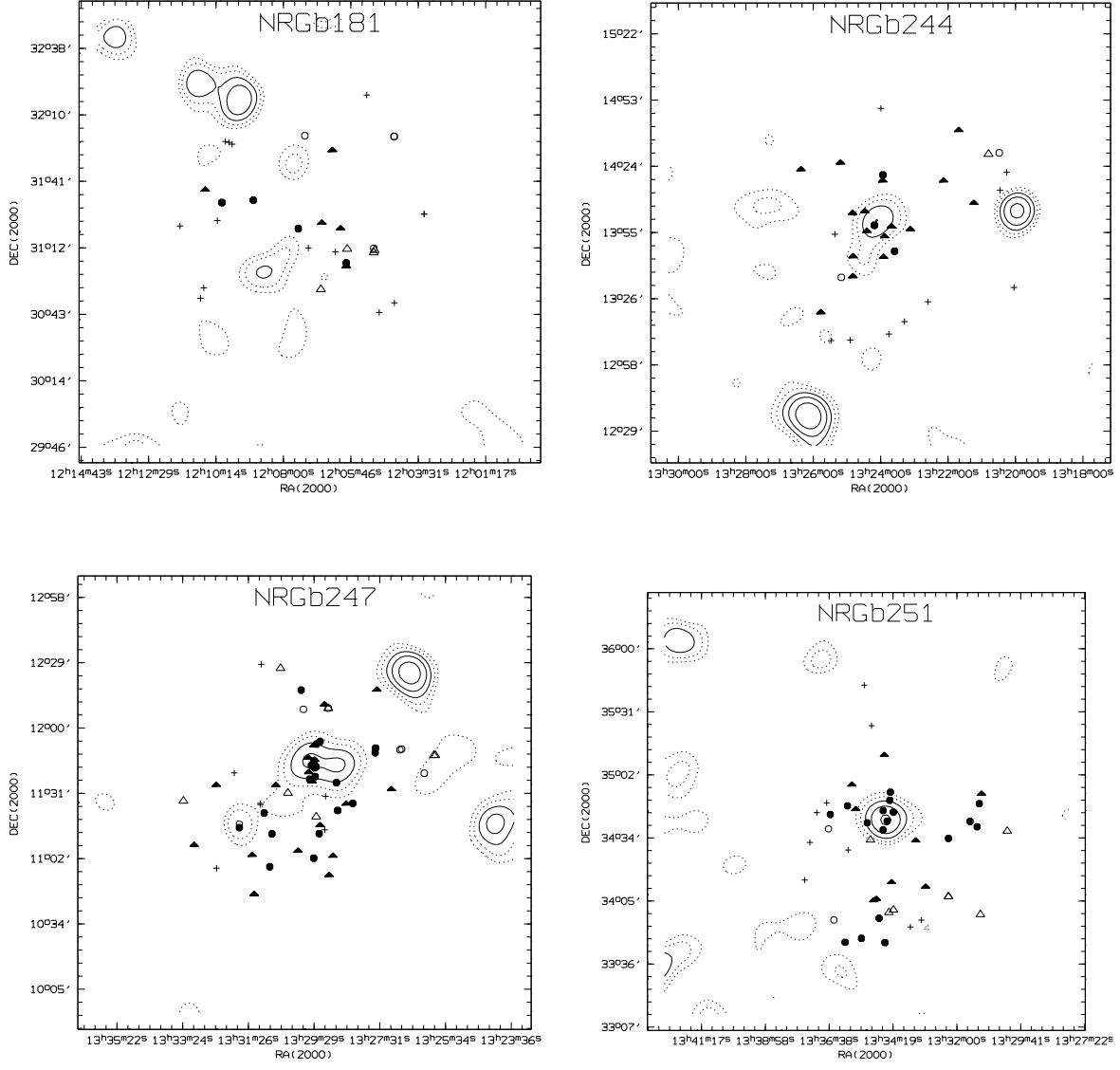


Fig. 5.— See caption for Figure 2.

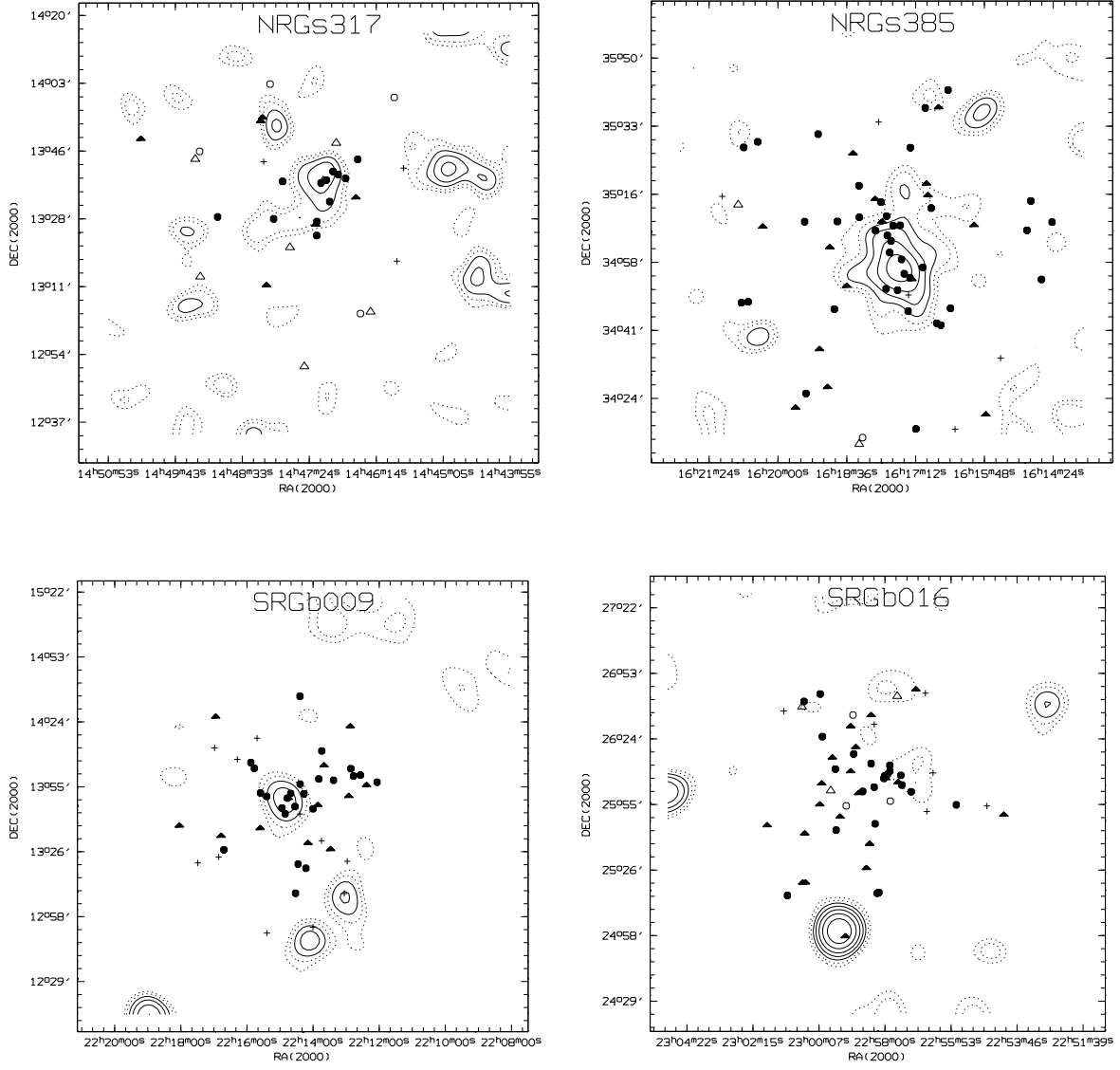


Fig. 6.— See caption for Figure 2.

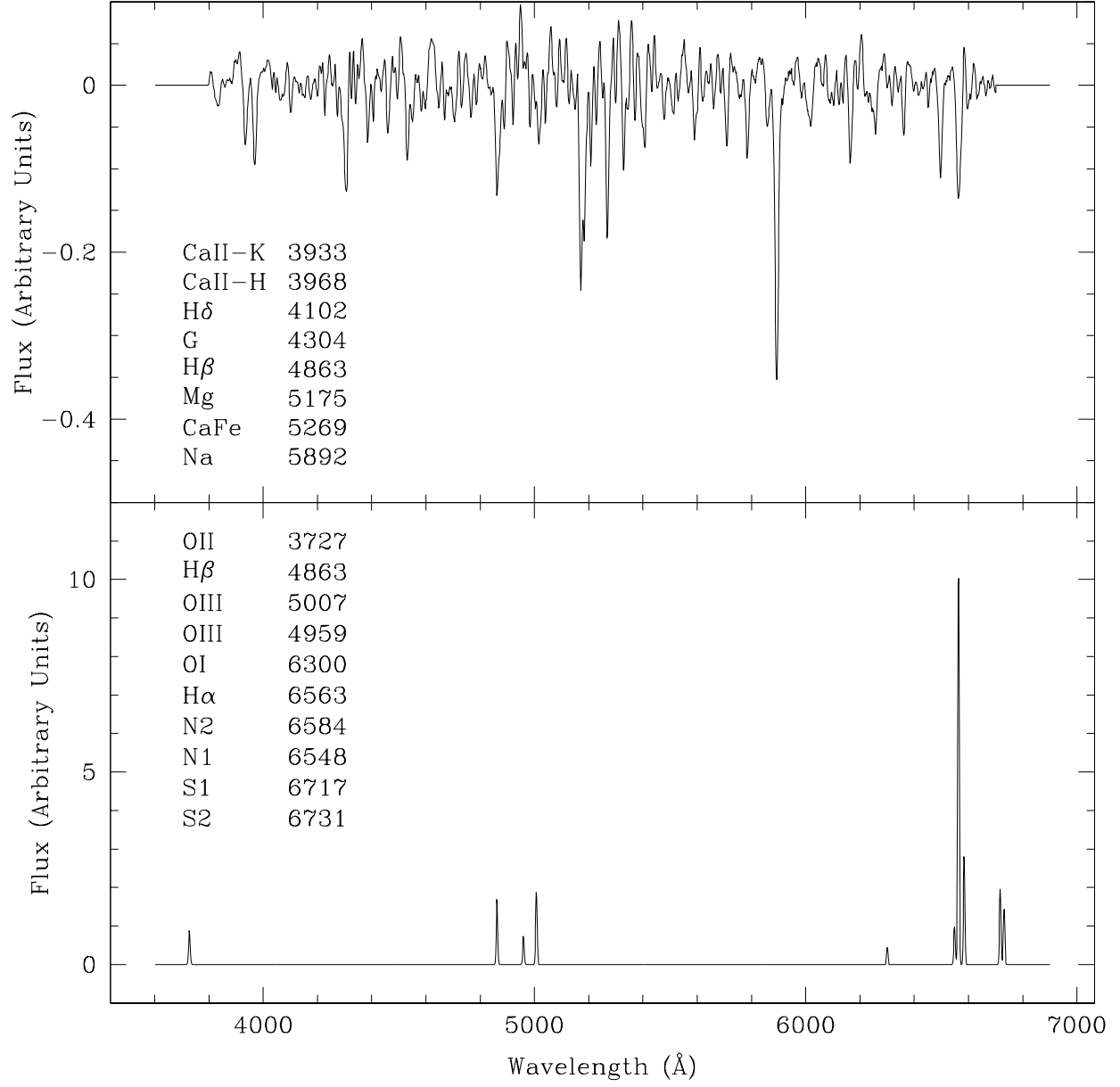


Fig. 7.— The absorption and emission spectral templates, with a list of the lines present.

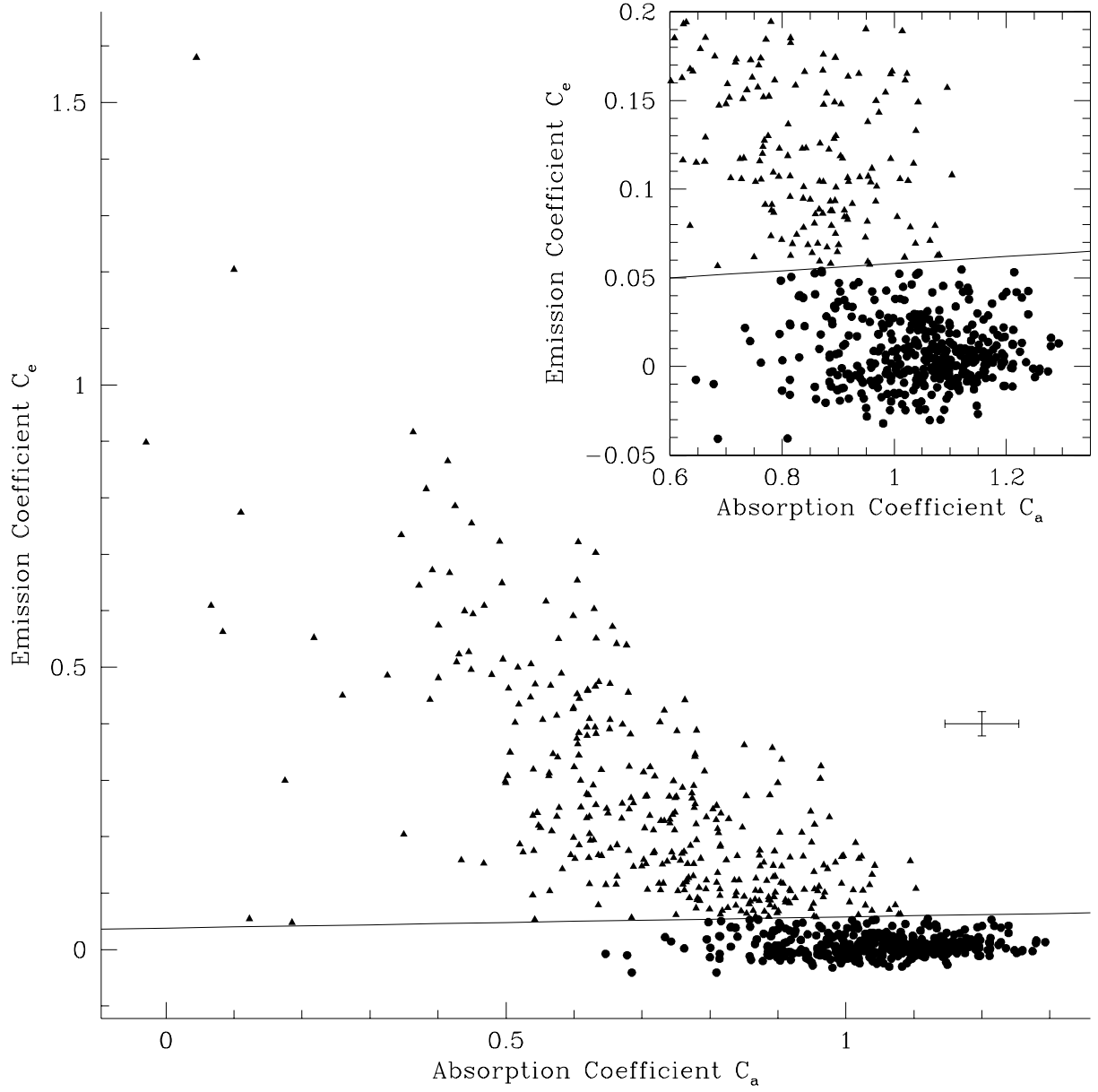


Fig. 8.— C_a vs. C_e for the 738 galaxies with $500 \text{ km s}^{-1} \leq cz \leq 15000 \text{ km s}^{-1}$. Triangles and circles represent emission-dominated and absorption-dominated galaxies, respectively. The errorbars show the typical uncertainty in the classification; the straight line is the maximum-likelihood dividing line described in the text. The top right box is a magnification of the absorption-dominated region.

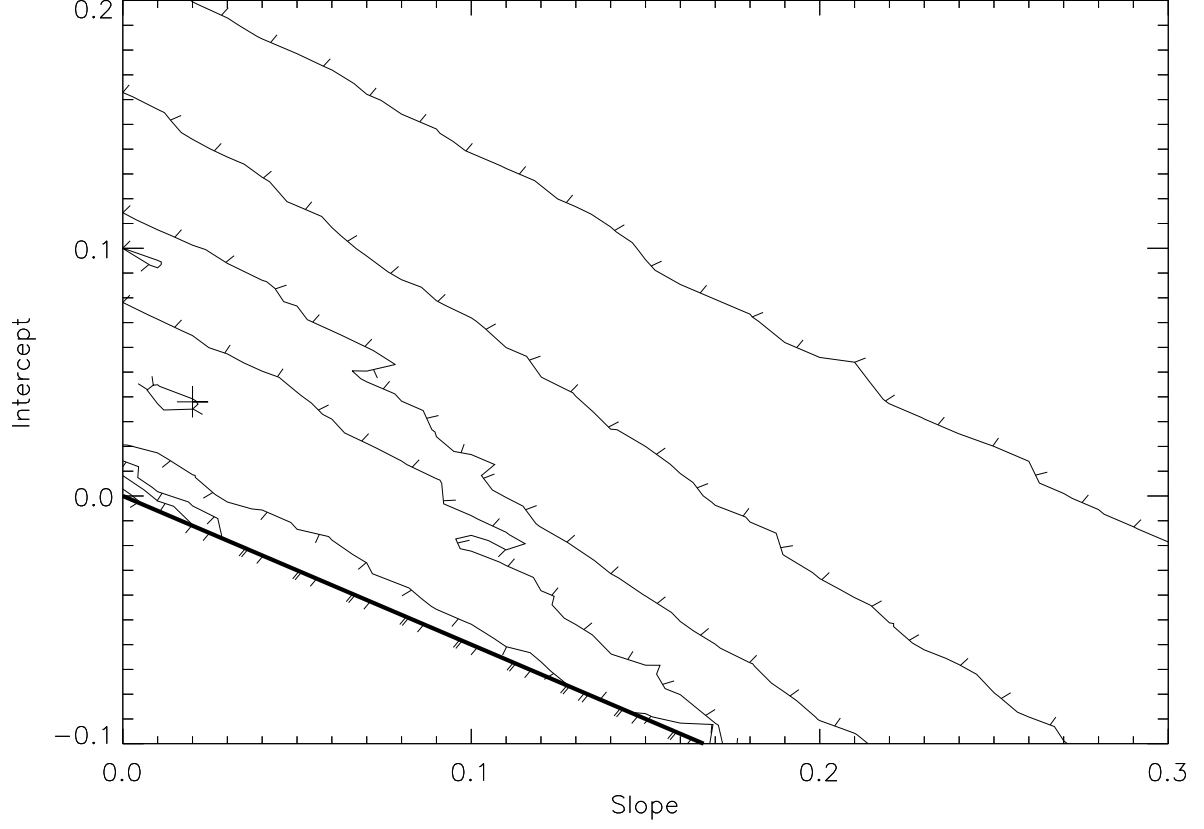


Fig. 9.— Maximization of the KS2D statistic (§C) for spectroscopic classification. Shown are contours of uniform $d_2 = 11, 12, 12.6, 13$, and 13.4 in the a - b (slope-intercept) plane. Tickmarks indicate the downhill direction, and the solid thick line indicates the $b > -0.6a$ boundary. The maximized value of d_2 is 13.44 ; a “+” marks its position.

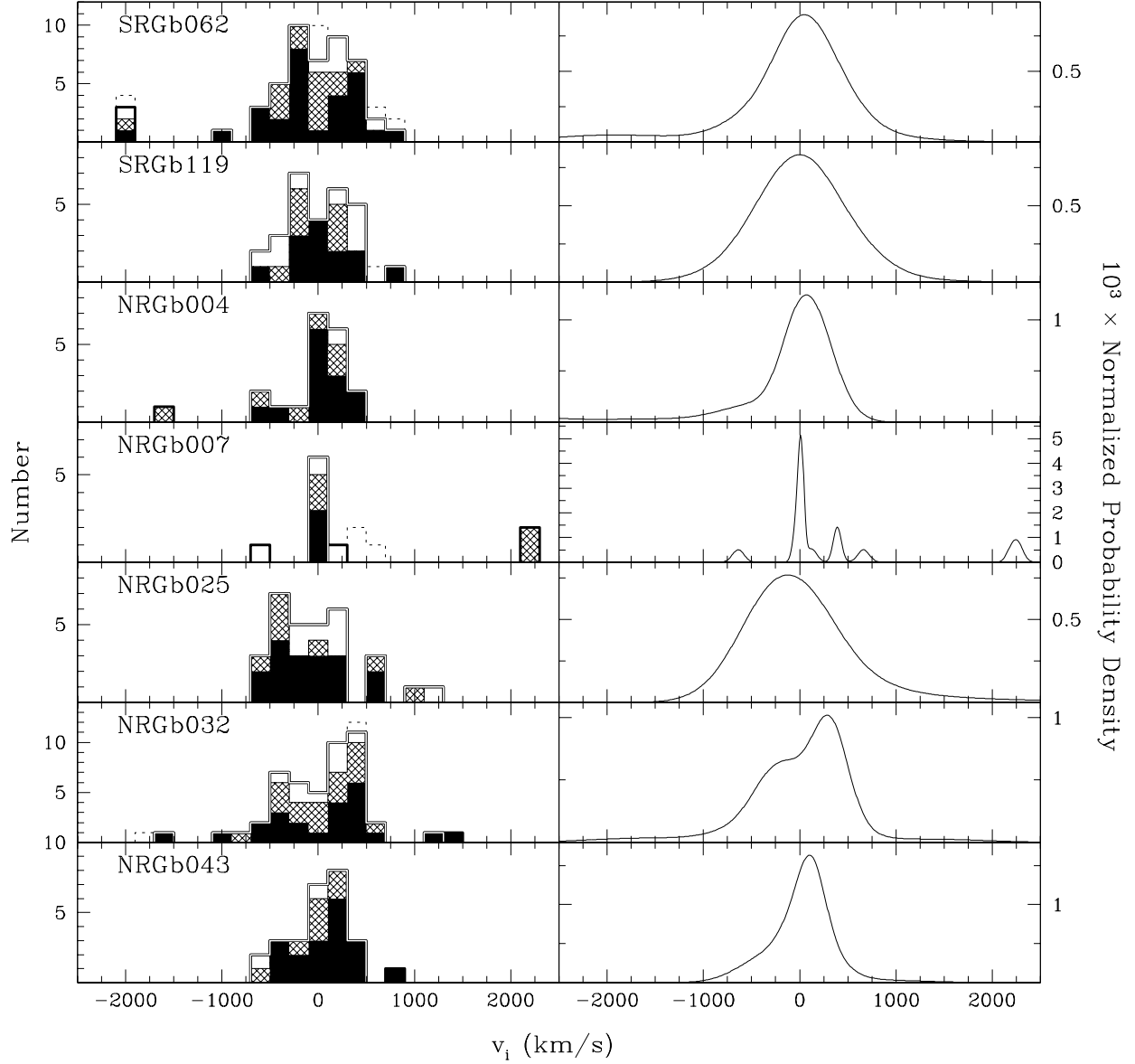


Fig. 10.— The distribution of v_i as defined in section §A. Histograms are coded (1) by line type: double-lined histograms show system members, heavy-lined histograms show foreground and background galaxies inside $1.5 h^{-1}$ Mpc of the system center, and dotted histograms show galaxies that are no longer inside this region after we recenter the system; (2) by shading: completely filled histograms show all galaxies within $0.5 h^{-1}$ Mpc of the system center, cross-hatched histograms those within $0.5 h^{-1}$ – $1.0 h^{-1}$ Mpc, and empty histograms those within $1.0 h^{-1}$ – $1.5 h^{-1}$ Mpc. On the right is a plot of f_{ka} as defined in equation (1).

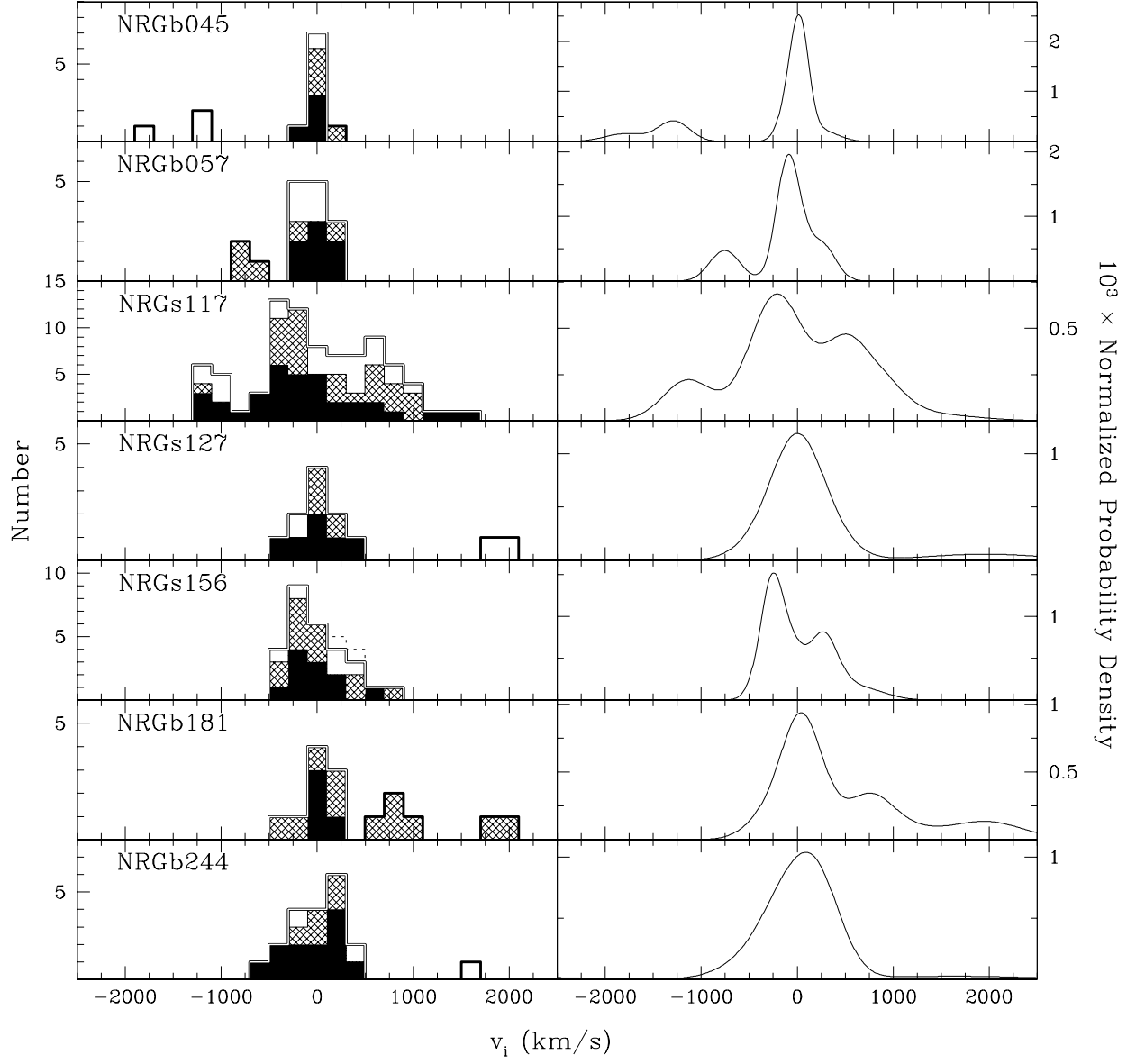


Fig. 11.— See caption for Figure 10.

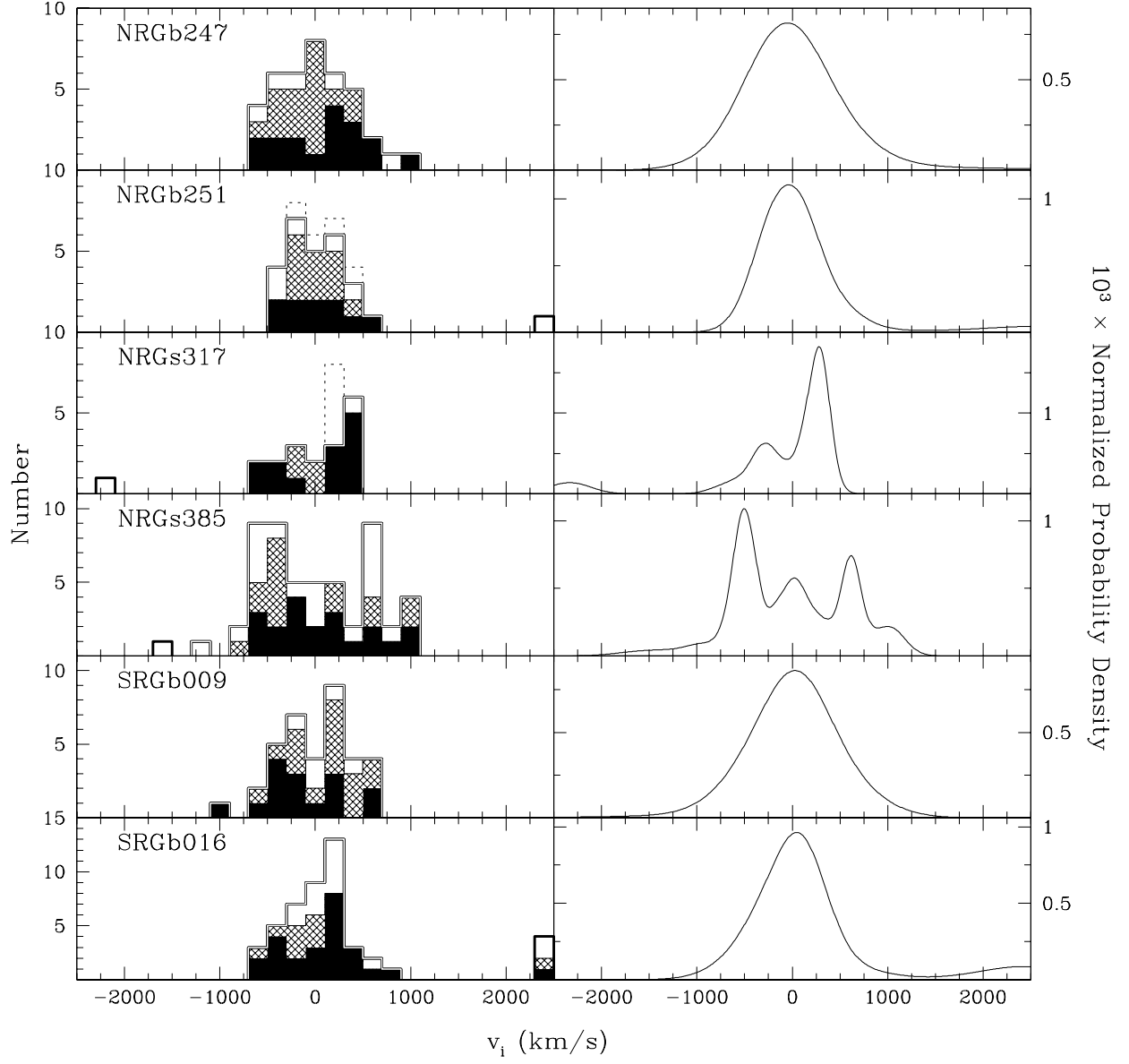


Fig. 12.— See caption for Figure 10.

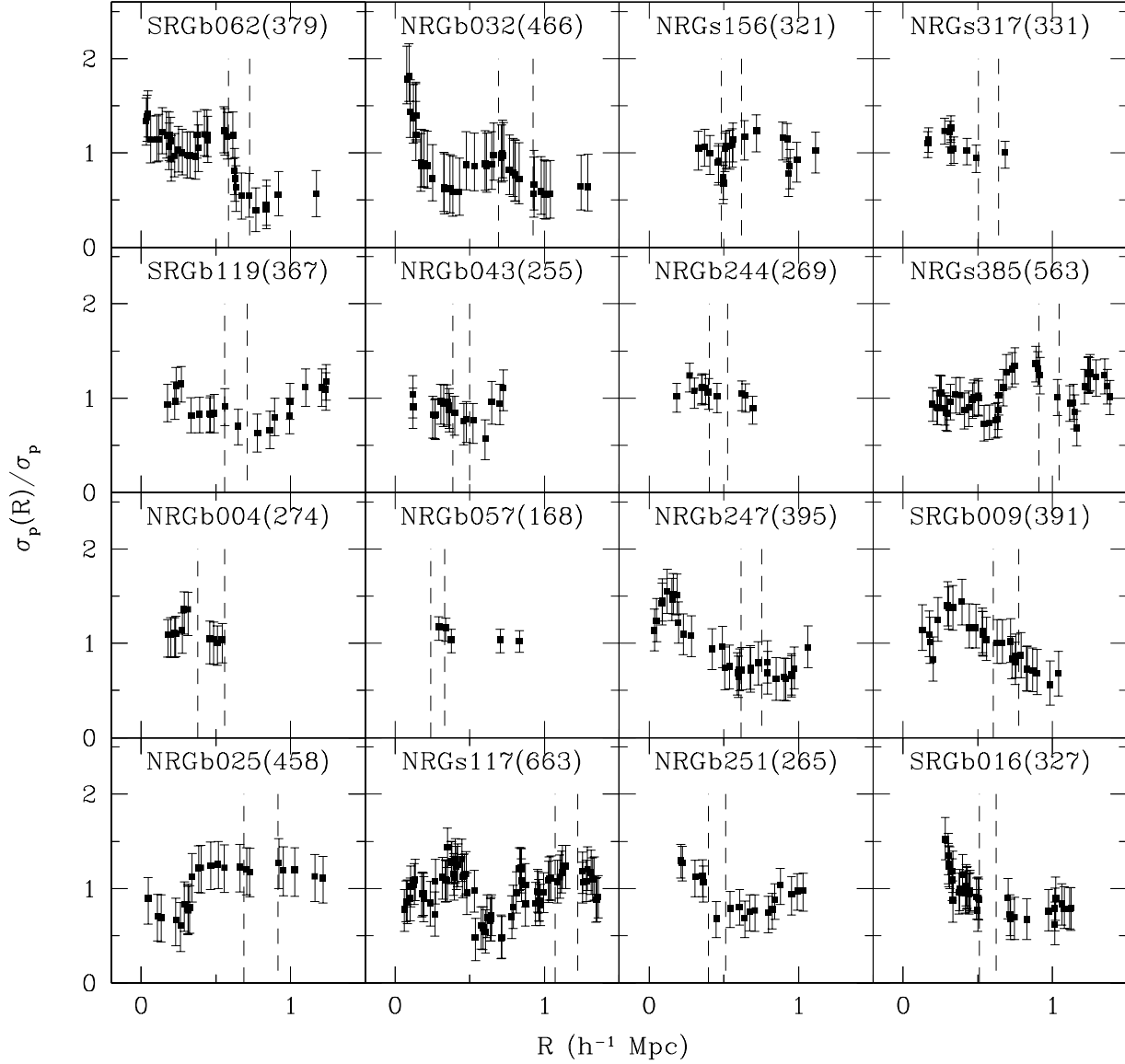


Fig. 13.— Velocity dispersion profiles. The error bars show the 68.3% bias-corrected bootstrap confidence intervals. The number in parenthesis indicates the global line-of-sight velocity dispersion σ_p in km s^{-1} . The dashed vertical lines show the 68.3% confidence interval for r_{200} as defined in equation (8).

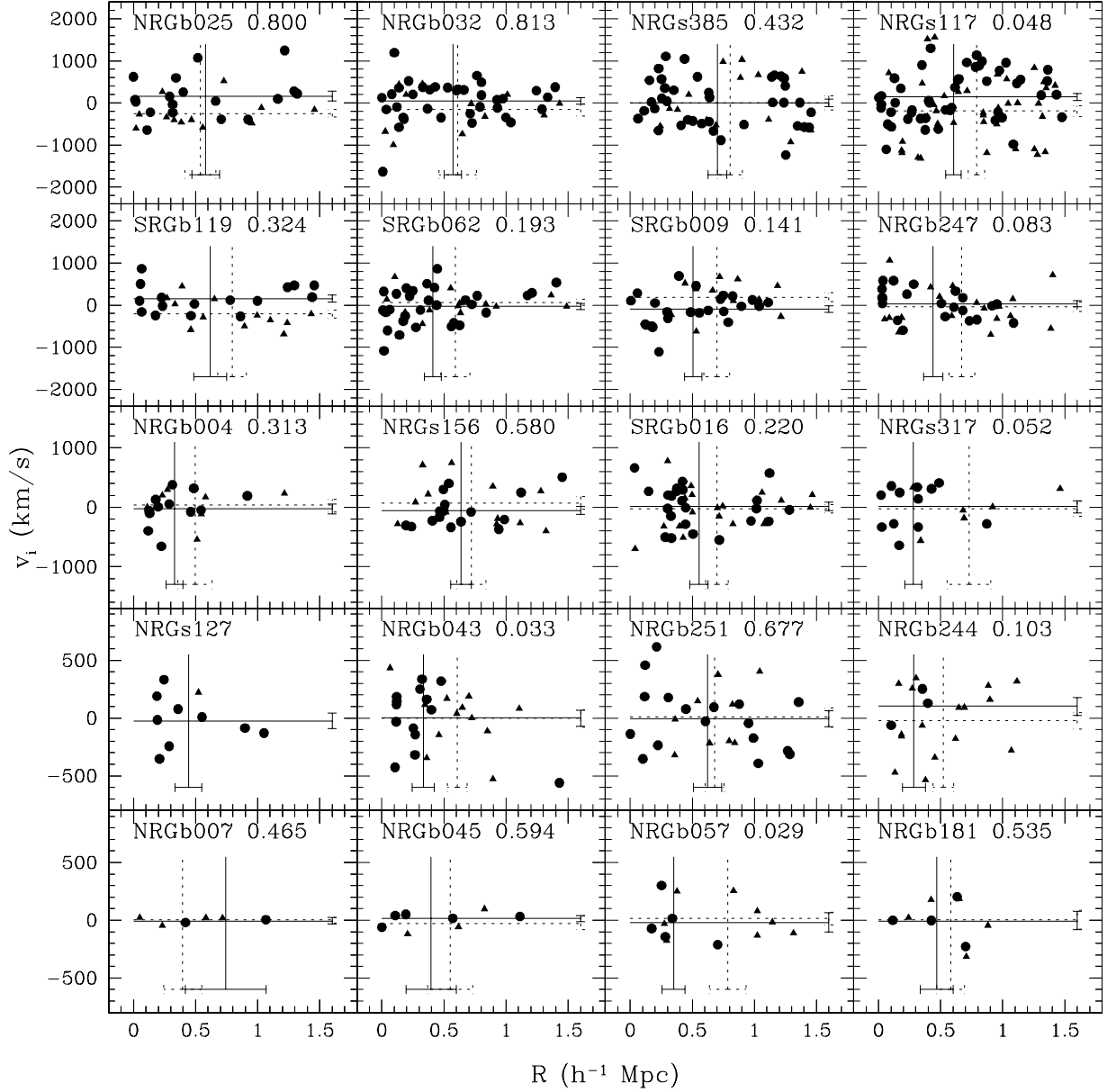


Fig. 14.— Velocity-distance diagrams. Dotted lines represent the mean projected distance and mean velocity of the emission-dominated galaxies (triangles), with accompanying errors; solid lines represent these quantities for absorption-dominated galaxies (circles). The number next to each system name is the probability, from the Student’s t test, that the emission-dominated and absorption-dominated galaxies have the same mean projected distance from the system center.

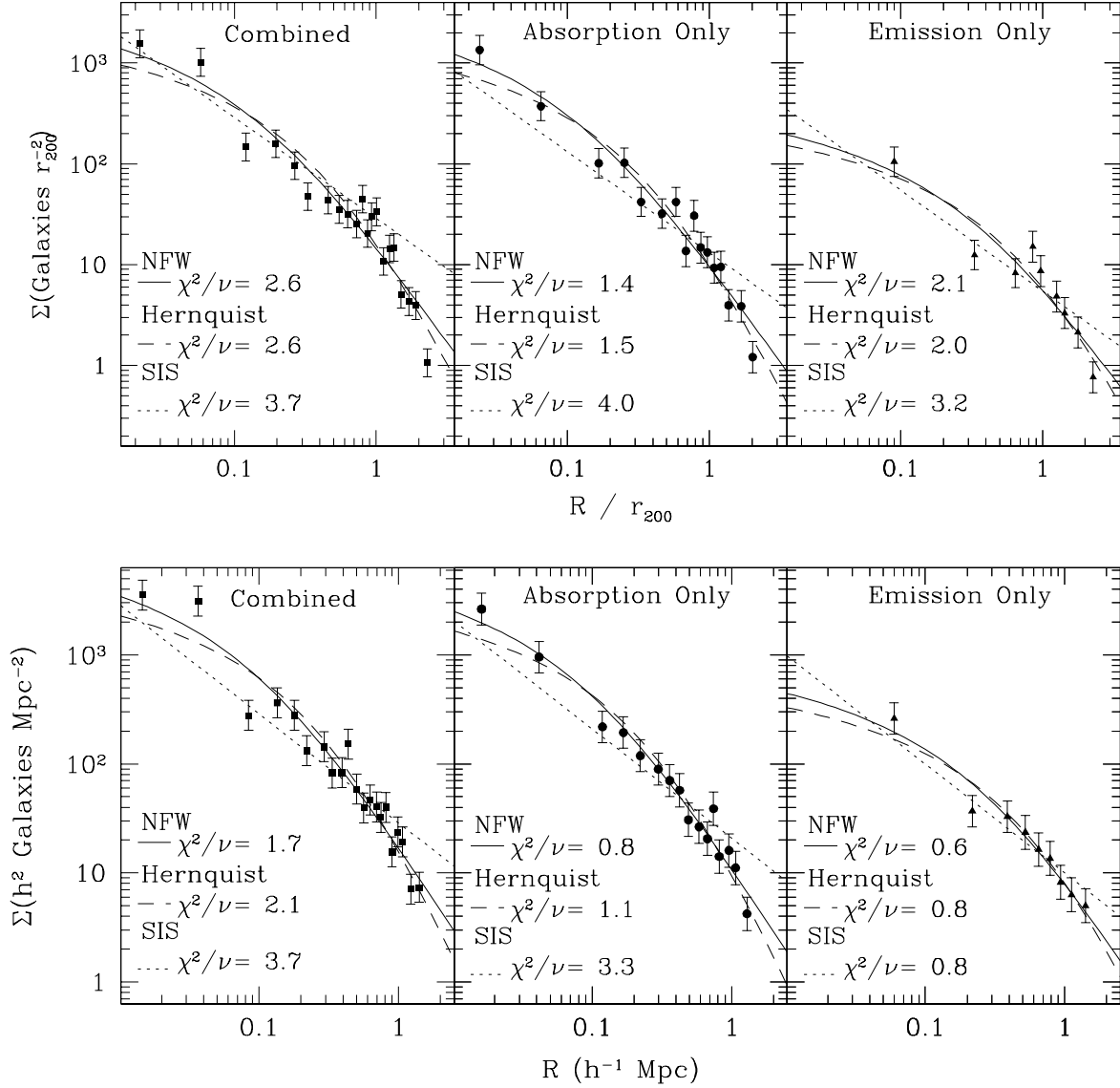


Fig. 15.— Surface number density profiles and best fit Hernquist (1990) NFW, and isothermal (SIS) profiles for Sample-D. The top panels show fits with R measured in units of r_{200} ; the bottom panels show fits with R in Mpc. From left to right we have (a) the fit to the combined emission- and absorption-dominated populations; (b) the fit to the absorption-dominated galaxies only; and (c) the fit to the emission-dominated galaxies only.

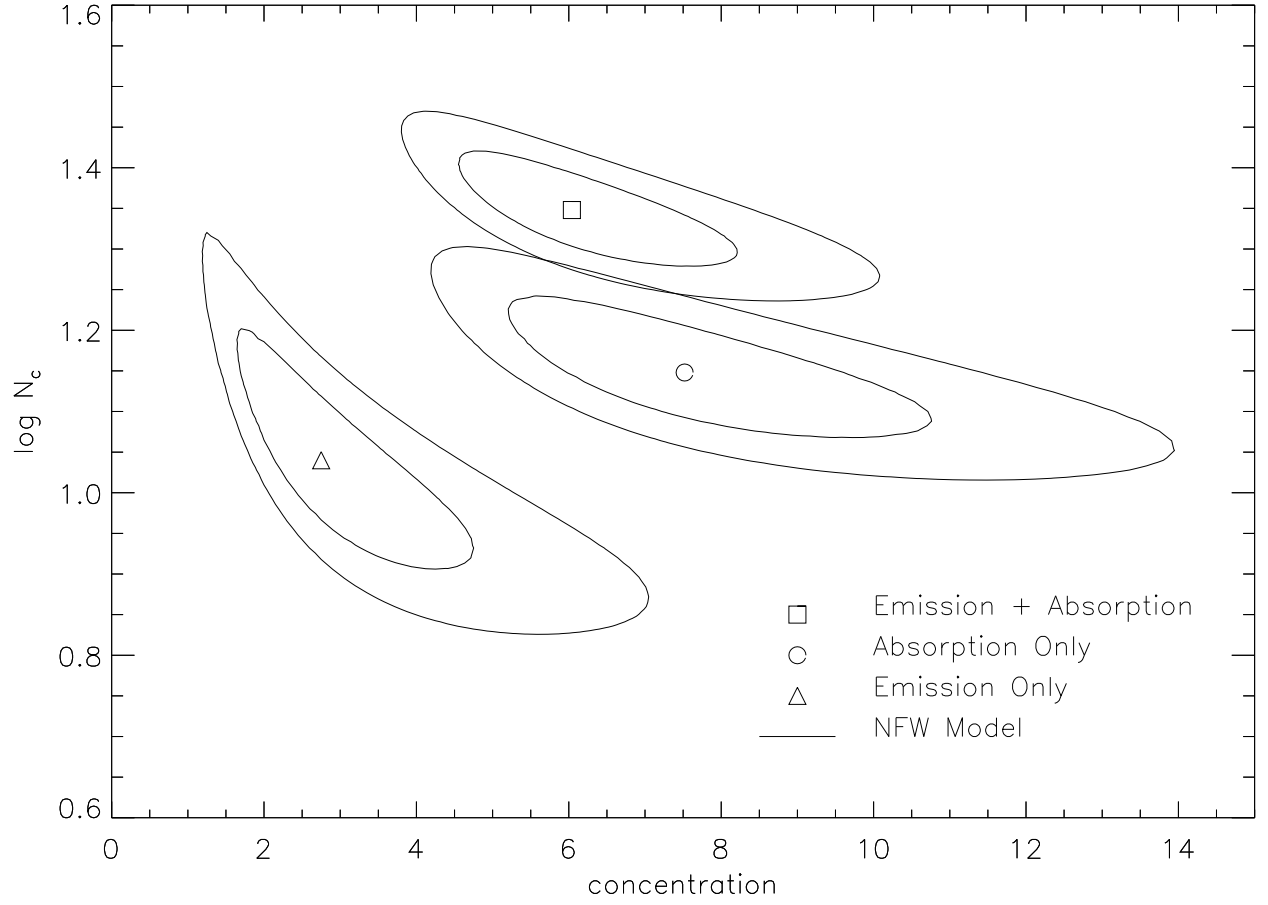


Fig. 16.— Contours of the 68.3% and 95.4% confidence regions for the fits in the top panel of figure 15.

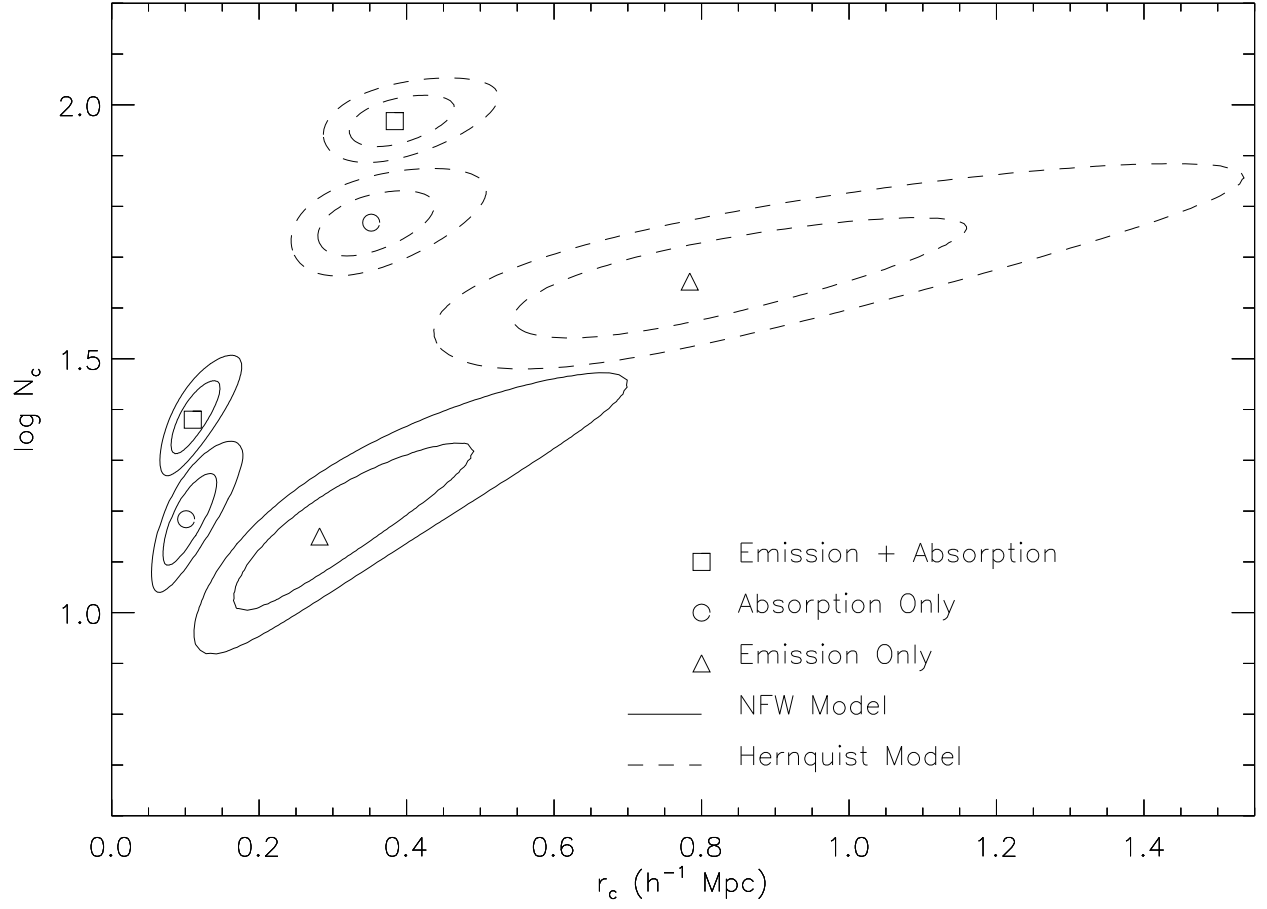


Fig. 17.— Contours of the 68.3% and 95.4% confidence regions for the fits in the bottom panel of figure 15.

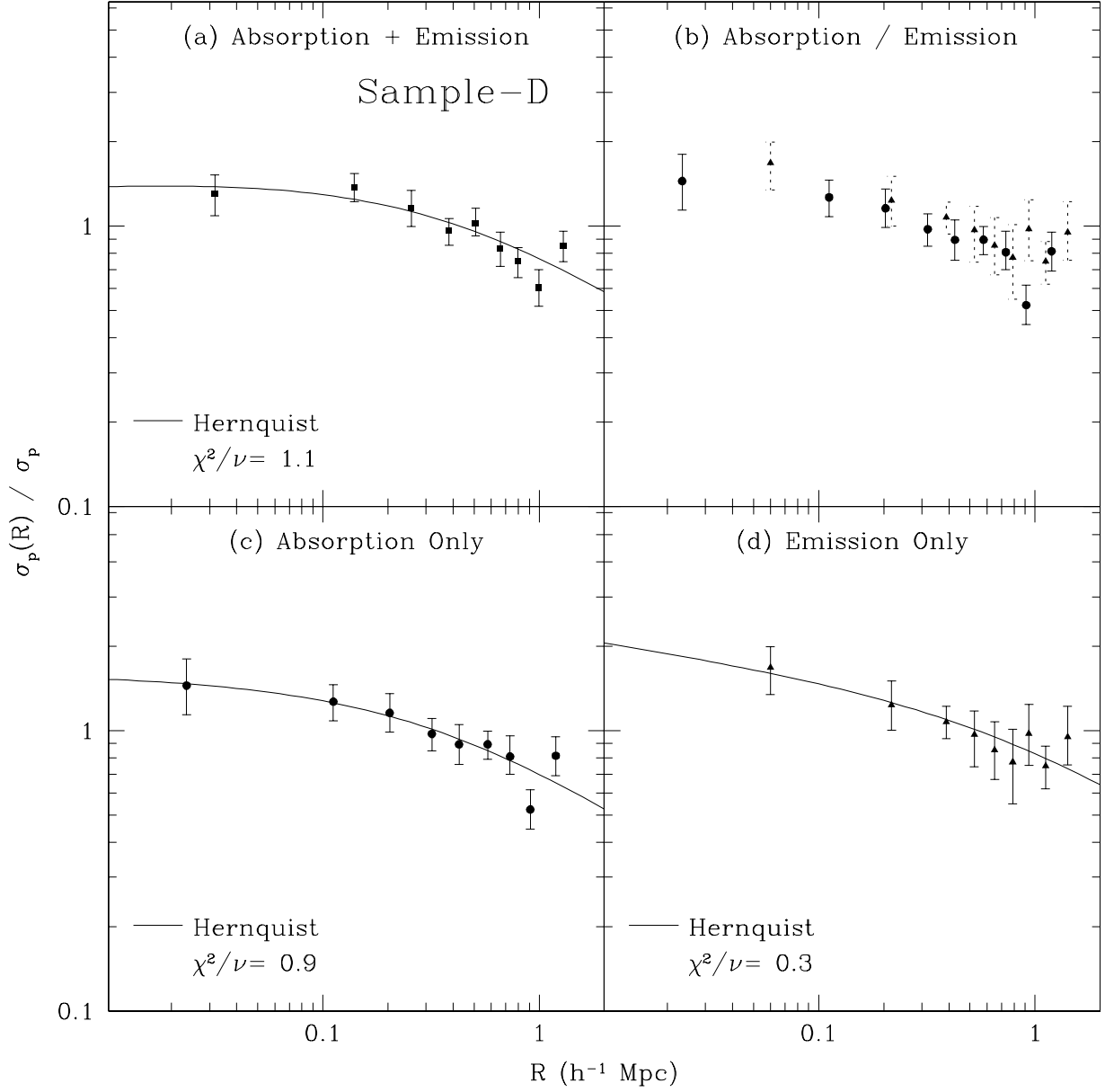


Fig. 18.— Fits of the line-of-sight velocity dispersion profile $\sigma_p(R)$ to the Hernquist (1990) model with constant β . Shown are (a) the fit to the combined emission- and absorption-dominated populations; (b) the two populations separately, where solid error bars represent the absorption- and dotted error bars represent the emission-dominated members; (c) the fit to the absorption-dominated galaxies only; (d) the fit to the emission-dominated galaxies only.

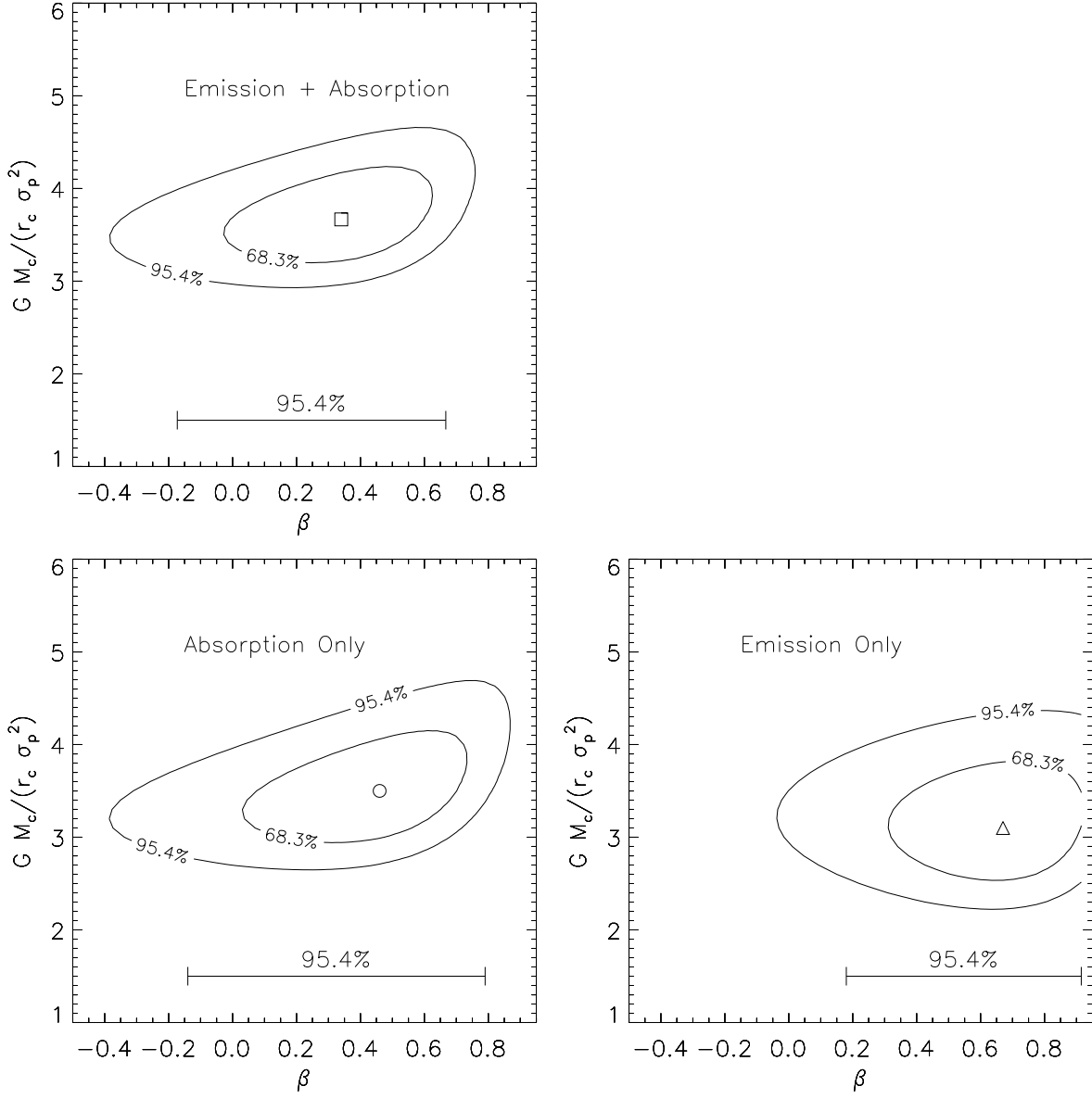


Fig. 19.— Confidence contours corresponding to the fits in figure 18.

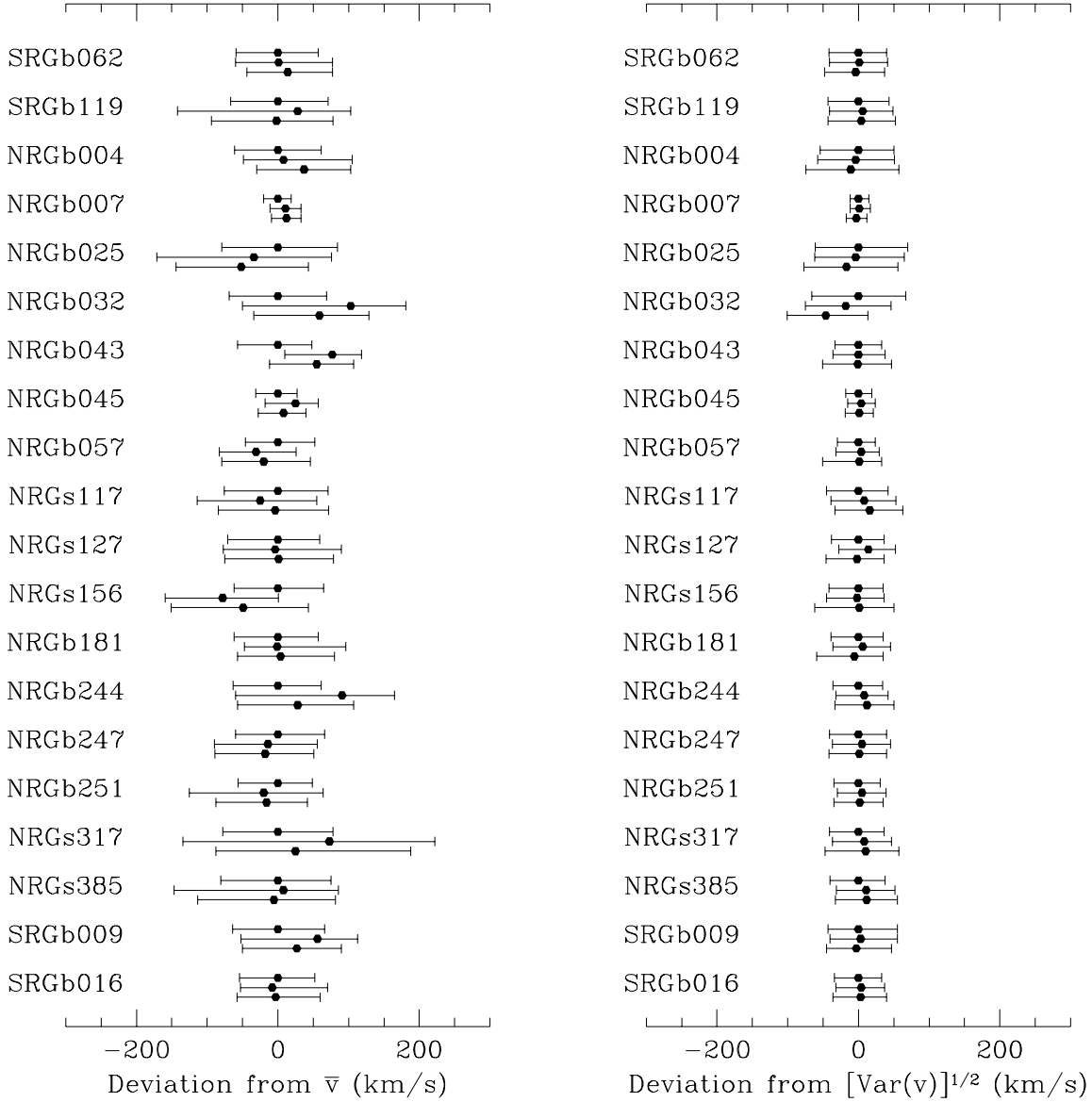


Fig. 20.— On the left for each system in our sample, we plot a stack of the three estimators of location, along with their 68.3% confidence intervals; shown are the mean (top), the median (middle), and the biweight (bottom). We shift the values for each system so that the mean is zero. Similarly, on the right we plot for each system a stack consisting of the standard deviation (top), the Gapper (middle), and the biweight (bottom) estimators of scale, shifted so that the standard deviation is zero.

Table 1. The Deep Optical Catalog: Basic Data

Group ID	α J2000	δ J2000	N CSOC	N Total	N DOC	$\langle v \rangle$ km s ⁻¹	σ_p km s ⁻¹	Comments	P point
SRGb062	00:18:22.5	30:04:00	13	84	45	6819 ⁺⁵⁷ ₋₅₉	379 ⁺⁴⁰ ₋₄₂	X,XC	< 0.001
SRGb119 ^a	01:56:13.8	05:35:12	8	54	28	5466 ⁺⁷¹ ₋₆₇	367 ⁺⁴³ ₋₄₃	X,XC	< 0.001
NRGb004	08:38:07.3	24:58:02	9	36	19	8559 ⁺⁶¹ ₋₆₁	274 ⁺⁵⁰ ₋₅₄	X,XC	0.587
NRGb007	08:50:29.9	36:29:13	6	39	6	7541 ⁺¹⁹ ₋₂₀	27 ⁺¹⁵ ₋₁₂	OC	...
NRGb025 ^{b,c}	09:13:37.3	29:59:58	5	35	31	6735 ⁺⁸⁴ ₋₇₉	458 ⁺⁷⁰ ₋₆₁	X,XC	< 0.001
NRGb032 ^{b,d}	09:19:46.9	33:45:00	5	67	47	6773 ⁺⁶⁹ ₋₆₉	466 ⁺⁶⁷ ₋₆₆	X,XC	< 0.001
NRGb043 ^b	09:28:16.2	29:58:08	5	30	26	7891 ⁺⁴⁸ ₋₅₇	255 ⁺³³ ₋₃₃	OC	...
NRGb045 ^b	09:33:25.6	34:02:52	5	26	8	8181 ⁺²⁷ ₋₃₁	70 ⁺¹⁹ ₋₁₈	X,XC	< 0.001
NRGb057 ^b	09:42:23.2	36:06:37	5	24	13	6766 ⁺⁵² ₋₄₆	168 ⁺²⁴ ₋₃₀	X,XC	0.684
NRGs117 ^{b,e}	11:10:42.9	28:41:38	14	89	84	9799 ⁺⁷¹ ₋₇₆	663 ⁺⁴² ₋₄₅	X,XC	< 0.001
NRGs127 ^b	11:21:34.2	34:15:31	8	12	10	10485 ⁺⁵⁹ ₋₇₁	206 ⁺³⁶ ₋₃₈	OC	...
NRGs156 ^b	11:44:54.5	33:15:17	7	35	28	9640 ⁺⁶⁵ ₋₆₂	321 ⁺³⁵ ₋₄₂	X,OC	0.111/0.210 ^f
NRGb181 ^b	12:07:35.5	31:26:32	6	18	9	6797 ⁺⁵⁷ ₋₆₂	176 ⁺³⁵ ₋₃₉	OC	...
NRGb244 ^a	13:23:57.9	14:02:37	7	32	19	6948 ⁺⁶¹ ₋₆₃	269 ⁺³⁴ ₋₃₆	X,XC	0.003
NRGb247	13:29:25.7	11:45:21	12	66	39	6851 ⁺⁶⁶ ₋₆₀	395 ⁺⁴⁰ ₋₄₁	X,XC	< 0.001
NRGb251	13:34:25.3	34:41:25	5	48	26	7346 ⁺⁴⁹ ₋₅₆	265 ⁺³¹ ₋₃₅	X,XC	< 0.001
NRGs317	14:47:05.3	13:39:46	11	46	18	8873 ⁺⁷⁸ ₋₇₈	331 ⁺³⁶ ₋₄₁	X,OC	0.055
NRGs385	16:17:43.9	34:58:00	8	61	53	9352 ⁺⁷⁵ ₋₈₀	563 ⁺³⁷ ₋₄₀	X,XC	< 0.001
SRGb009	22:14:46.0	13:50:30	8	46	36	7744 ⁺⁶⁶ ₋₆₄	391 ⁺⁵⁵ ₋₄₃	X,XC	< 0.001
SRGb016	22:58:45.9	26:00:05	6	58	43	7395 ⁺⁵² ₋₅₄	327 ⁺³³ ₋₃₄	X,OC	< 0.001

Note. — N_{CSOC} is the number of galaxies classified as members in the CSOC; N_{Total} is the total number of galaxies to $m_R \approx 15.4$ in the field of the system; N_{DOC} is the total number of galaxies classified as members in this work. P_{point} is the probability that the x-ray emission in the field is due to a single point source. Letters in the “comments” column denote the following. X: has x-ray emission. XC: Position quoted is the x-ray centroid. OC: Position quoted is the mean optical position.

^a Also studied by Zabludoff & Mulchaey (1998).

^b Also studied by Ramella et al. (1995).

^c Contains Hickson Compact Group 37 (Hickson 1982).

^d Abell 779 (Abell 1958).

^e Abell 1185 (Abell 1958).

^f Probabilities for the south and the north x-ray emission peaks coincident with member galaxies, respectively.

Table 2. Galaxy Positions and Measured Velocities

Galaxy ID	α_{2000}	δ_{2000}	Cz_i
SRGb062.01	00:11:57.0	+29:29:08	28038
SRGb062.02	00:12:11.8	+29:19:09	7728
SRGb062.03	00:12:17.5	+29:52:17	6921
SRGb062.04	00:12:28.4	+29:32:38	6862
SRGb062.05	00:12:38.3	+30:06:08	6791
SRGb062.06	00:12:45.0	+29:22:15	10419
SRGb062.07	00:13:12.7	+31:08:43	14465
SRGb062.08	00:13:45.1	+30:11:40	7109
SRGb062.09	00:13:55.9	+28:45:47	6908
SRGb062.10	00:13:57.2	+30:52:55	4782
SRGb062.11	00:14:01.9	+29:25:57	7055
SRGb062.12	00:14:13.7	+28:52:36	7333
SRGb062.13	00:14:55.2	+31:06:12	24282
SRGb062.14	00:15:07.6	+28:52:29	38145
SRGb062.15	00:15:15.6	+29:21:44	7046
SRGb062.16	00:15:22.2	+29:39:42	6790
SRGb062.17	00:15:23.1	+30:43:14	14292
SRGb062.18	00:15:24.7	+29:38:48	21460
SRGb062.19	00:15:28.8	+30:43:23	13890
SRGb062.20	00:15:43.9	+29:39:58	6642
...

Note. — This is a sample listing; the full table is available electronically. All velocities are in km s^{-1} ; the typical uncertainty is 40 km s^{-1} .

Table 3. Kolmogorov-Smirnov Tests for $\sigma(R)$

	(01)	(02)	(03)	(04)	(05)	(06)	(07)	(08)	(09)	(10)	(11)	(12)	(13)	(14)	(15)
SRGb062(01)	...	**	*	*	***	***	***	**	*	*	***	*	***	*	**
SRGb119(02)	**	...	***	**	*	*	*	*	***	*	*	***	*	*	*
NRGb004(03)	*	***	...	**	***	***	***	***	*	**	**	*	***	*	***
NRGb025(04)	*	***	*	...	***	***	***	***	**	***	***	*	**	***	***
NRGb032(05)	**	*	***	***	...	***	***	***	***	*	*	***	***	**	**
NRGb043(06)	***	*	***	***	*	...	***	***	***	***	**	***	***	***	**
NRGs117(07)	*	**	*	**	***	***	...	*	***	***	*	**	*	***	**
NRGs156(08)	***	*	**	***	***	**	***	...	**	***	*	**	*	*	***
NRGb244(09)	**	***	*	**	***	***	*	*	...	**	**	*	**	*	**
NRGb247(10)	*	*	**	***	*	*	***	***	***	...	*	**	***	*	*
NRGb251(11)	***	*	***	***	***	**	***	*	**	**	...	**	*	*	*
NRGs317(12)	*	***	*	*	***	***	*	**	*	*	**	...	***	*	*
NRGs385(13)	**	***	**	*	***	***	*	***	**	***	***	*	...	*	***
SRGb009(14)	*	*	*	***	***	**	**	**	*	*	**	*	***	...	*
SRGb016(15)	***	*	**	***	***	*	***	***	**	*	*	*	***	*	...

Note. — The results for R measured in units of Mpc are above and to the right of the dividing diagonal, while those for R in units of r_{200} are below and to the left. For each unique pair of systems, the null hypothesis that $\sigma(R)$ is drawn from the same distribution is rejected (1) at less than the 95.4% confidence level if there is only one star; (2) at better than the 95.4% confidence level if there are two stars; (3) at better than the 99.0% confidence level if there are three stars; and (4) at better than the 99.9% confidence level if there are four stars.

Table 4. Comparison of Absorption- and Emission-Dominated Populations

Group	f_{abs}	$P(F)$	Velocity			Projected Distance			
			σ_p^a/σ_p^e	$P(t)$	$\frac{\langle v \rangle^a - \langle v \rangle^e}{\sigma_p}$	$P(F)$	$\sqrt{\frac{\text{Var}(R^a)}{\text{Var}(R^e)}}$	$P(t)$	$\bar{R}^a - \bar{R}^e$ $h^{-1} \text{ Mpc}$
SRGb062 ^D	0.689	0.129	1.49 ± 0.35	0.378	-0.25 ± 0.29	0.436	0.85 ± 0.05	0.193	-0.18 ± 0.15
SRGb119	0.571	0.805	0.94 ± 0.22	0.009	1.00 ± 0.37	0.343	1.33 ± 0.04	0.324	-0.18 ± 0.19
NRGb004	0.632	0.914	0.99 ± 0.55	0.682	-0.21 ± 0.55	0.201	0.65 ± 0.23	0.313	-0.16 ± 0.16
NRGb007	0.333	0.727	0.52 ± 0.87	0.629	-0.37 ± 1.51	0.466	1.49 ± 1.55	0.465	0.35 ± 0.35
NRGb025	0.613	0.264	1.39 ± 0.46	0.009	0.90 ± 0.36	0.720	1.12 ± 0.08	0.800	0.04 ± 0.18
NRGb032 ^D	0.766	0.804	0.96 ± 0.26	0.231	0.44 ± 0.38	0.406	0.83 ± 0.03	0.813	-0.04 ± 0.16
NRGb043	0.538	0.775	1.09 ± 0.32	0.981	0.01 ± 0.42	0.543	1.20 ± 0.55	0.033	-0.27 ± 0.13
NRGb045	0.625	0.110	0.39 ± 0.26	0.587	0.61 ± 1.02	0.699	1.44 ± 0.56	0.594	-0.15 ± 0.25
NRGb057	0.385	0.636	1.20 ± 0.64	0.746	-0.21 ± 0.62	0.199	0.48 ± 0.24	0.029	-0.40 ± 0.18
NRGs117	0.560	0.069	0.75 ± 0.10	0.036	0.49 ± 0.24	0.725	1.06 ± 0.01	0.048	-0.19 ± 0.09
NRGs156	0.571	0.225	0.71 ± 0.17	0.339	-0.40 ± 0.41	0.447	0.81 ± 0.06	0.580	-0.08 ± 0.15
NRGb181	0.444	0.841	0.86 ± 0.50	0.929	-0.07 ± 0.68	0.883	1.06 ± 0.27	0.535	-0.11 ± 0.16
NRGb244	0.158	0.503	0.55 ± 0.24	0.328	0.47 ± 0.42	0.407	0.48 ± 0.29	0.103	-0.24 ± 0.12
NRGb247 ^D	0.538	0.162	0.72 ± 0.15	0.603	0.18 ± 0.34	0.321	0.79 ± 0.02	0.083	-0.23 ± 0.13
NRGb251	0.654	0.931	1.05 ± 0.26	0.896	-0.05 ± 0.42	0.046	2.04 ± 0.09	0.677	-0.06 ± 0.14
NRGs317	0.667	0.935	1.07 ± 0.36	0.844	0.11 ± 0.50	0.096	0.56 ± 0.15	0.052	-0.45 ± 0.19
NRGs385	0.717	0.489	0.87 ± 0.13	0.985	-0.01 ± 0.33	0.507	1.18 ± 0.02	0.432	-0.10 ± 0.12
SRGb009 ^D	0.667	0.819	0.96 ± 0.25	0.055	-0.71 ± 0.36	0.785	1.02 ± 0.05	0.141	-0.14 ± 0.12
SRGb016 ^D	0.535	0.862	1.04 ± 0.21	0.696	0.13 ± 0.33	0.532	0.87 ± 0.04	0.220	-0.15 ± 0.12
ALL	0.602	0.197	0.93 ± 1.96	0.129	0.13 ± 3.27	0.553	1.04 ± 0.00	0.000	-0.14 ± 0.03
Sample-A	0.609	0.519	0.96 ± 2.16	0.454	0.07 ± 3.58	0.546	1.04 ± 0.00	0.000	-0.13 ± 0.04
Sample-D	0.646	0.819	0.98 ± 0.11	0.799	-0.04 ± 0.16	0.266	0.89 ± 0.01	0.010	-0.15 ± 0.06
Sample-I	0.585	0.474	0.94 ± 2.75	0.258	0.14 ± 4.66	0.088	1.16 ± 0.01	0.015	-0.11 ± 0.05

Note. — The fraction of absorption-dominated galaxies in each system is f_{abs} . A low value of $P(t)$ indicates that two populations have significantly different means; a low value of $P(F)$ indicates that they have significantly different variances. Sample-A consists of all systems except NRGs117; Sample-D contains the systems with declining line-of-sight velocity dispersion profile, marked with a superscript “D”; Sample-I consists of all systems except those in Sample-D and NRGs117.

Table 5. Surface Density Profiles

Spectral Class	N_{gal}	NFW ^a		NFW ^b		Hernquist ^b		Isothermal ^b
		χ^2/ν	c	χ^2/ν	r_c	χ^2/ν	r_c	χ^2/ν
Sample-D ^c ; $\sigma_p = 327\text{--}466 \text{ km s}^{-1}$.								
Absorption	135	1.4	4.9–12	0.8	0.062–0.16	1.1	0.26–0.46	3.3
Emission	75	2.1	1.4–5.6	0.60	0.14–0.58	0.79	0.50–1.3	0.79
Combined	210	2.6	4.3–9.1	1.7	0.074–0.16	2.1	0.30–0.49	3.7
8 Groups with $\sigma_p > 350 \text{ km s}^{-1}$.								
Absorption	232	2.4	7.6–16	1.0	0.067–0.14	2.0	0.30–0.46	3.1
Emission	131	1.5	1.6–4.4	1.0	0.29–0.69	1.1	0.81–1.8	0.9
Combined	363	2.5	4.3–7.7	1.3	0.12–0.22	2.4	0.45–0.65	2.2
9 Groups ^d with $\sigma_p < 350 \text{ km s}^{-1}$.								
Absorption	102	5.7	†	4.5	†	3.7	†	8.8
Emission	92	3.8	†	2.5	0.17–0.59	2.2	0.52–1.53	3.5
Combined	192	4.2	†	3.0	0.12–0.30	2.5	0.39–0.59	5.1

Note. — We list the 95.4% confidence interval for each fit parameter. N_{gal} is the total number of galaxies used in each fit. The core radius r_c is always in units of $h^{-1} \text{ Mpc}$.

^aFit with projected radius R in units of r_{200}^{Virial} .

^bFit with projected radius R in units of Mpc.

^cThe 5 Systems with Declining $\sigma_p(R)$.

^dIncludes only systems with > 10 members.

†This fit is ruled out with high confidence ($\chi^2/\nu > 3.5$).